

1
2
3
4
5
6
7
8
9
10
11
12
13
14
15
16
17
18
19
20
21
22
23
24
25
26
27
28
29
30
31
32
33
34
35
36
37
38
39
40
41
42
43
44

**Composite synoptic-scale environments conducive to North American polar/subtropical jet
superposition events**

By

ANDREW C. WINTERS^{1*}, DANIEL KEYSER², LANCE F. BOSART², and JONATHAN E.
MARTIN³

¹Department of Atmospheric and Oceanic Sciences
University of Colorado Boulder
Boulder, CO 80309

²Department of Atmospheric and Environmental Sciences
University at Albany, State University of New York
Albany, NY 12222

³Department of Atmospheric and Oceanic Sciences
University of Wisconsin – Madison
Madison, WI 53706

Submitted for publication in *Monthly Weather Review*
XX August 2019

* *Corresponding author address:* Andrew C. Winters, Dept. of Atmospheric and Oceanic Sciences, University of Colorado Boulder, Street Address., Boulder, CO 12222. E-mail: acwinters@albany.edu

45 ABSTRACT

46
47 While the Northern Hemisphere polar and subtropical jet streams typically reside in different
48 climatological latitude bands, the separation between the two jets occasionally vanishes resulting
49 in a polar/subtropical jet superposition. The development of a jet superposition represents the
50 creation of a dynamical and thermodynamic environment that is particularly conducive to the
51 production of high-impact weather. The synoptic-scale environments that support the
52 development of North American jet superpositions can vary considerably, however, depending
53 on the case under consideration. This observation motivates a comprehensive examination of the
54 varied synoptic-dynamic mechanisms that operate within a double-jet environment to produce
55 North American jet superpositions. This study objectively identifies North American jet
56 superposition events during November–March 1979–2010 and subsequently classifies those
57 events into three characteristic event types. “Polar dominant” events are those during which only
58 the polar jet is characterized by a substantial excursion from its climatological latitude band,
59 “subtropical dominant” events are those during which only the subtropical jet is characterized by
60 a substantial excursion from its climatological latitude band, and “hybrid” events are those
61 characterized by a mutual excursion of both jets from their respective climatological latitude
62 bands. Composite analyses performed on each event type reveal the important role that descent
63 plays in restructuring the tropopause beneath the confluent jet-entrance region prior to each jet
64 superposition event type. Additionally, surface cyclogenesis and implied diabatic processes tend
65 to lead and directly contribute to the development of subtropical dominant superpositions, while
66 those processes tend to maximize concurrently with and downstream of polar dominant
67 superpositions.

68 **1. Introduction**

69 The instantaneous positions of the polar and subtropical jets are closely related to the
70 pole-to-equator tropopause structure (e.g., Defant and Taba 1957; Palmén and Newton 1969;
71 Shapiro et al. 1987). In the Northern Hemisphere, the polar jet is located near 50°N in the region
72 where the tropopause height abruptly rises from the polar tropopause (~350 hPa) to the
73 subtropical tropopause (~250 hPa). The polar jet sits atop the strongly baroclinic, tropospheric-
74 deep polar front (e.g., Palmén and Newton 1948; Namias and Clapp 1949; Newton 1954; Palmén
75 and Newton 1969, Keyser and Shapiro 1986; Shapiro and Keyser 1990) and arises due to the
76 eddy momentum flux convergence that accompanies developing baroclinic waves (e.g., Held
77 1975; Rhines 1975; McWilliams and Chow 1981; Panetta 1993). The subtropical jet is located
78 equatorward of the polar jet near 30°N in the region where the tropopause height abruptly rises
79 from the subtropical tropopause to the tropical tropopause (~100 hPa). The subtropical jet
80 features modest baroclinicity in the upper troposphere and lower stratosphere, and arises due to
81 the poleward transport of angular momentum by the Hadley circulation (e.g., Loewe and Radok
82 1950; Yeh 1950; Koteswaram 1953; Mohri 1953; Koteswaram and Parthasarathy 1954; Sutcliffe
83 and Bannon 1954; Krishnamurti 1961; Riehl 1962; Held and Hou 1980).

84 While the polar and subtropical jets typically occupy separate climatological latitude
85 bands, the latitudinal separation between the two jet streams occasionally vanishes resulting in a
86 polar/subtropical jet superposition (e.g., Winters and Martin 2014, 2016, 2017; Handlos and
87 Martin 2016; Christenson et al. 2017). A cross section perpendicular to the axis of an observed
88 jet superposition at 1200 UTC 20 December 2009 highlights the leading characteristics of a jet
89 superposition (Figs. 1a,b). These characteristics include the development of (1) a steep, two-step
90 pole-to-equator tropopause structure, (2) anomalously strong wind speeds that can exceed 100 m

91 s^{-1} in some instances, and (3) strong baroclinicity in the upper troposphere and lower
92 stratosphere as required by thermal wind balance. The development of strong baroclinicity
93 attendant to the jet superposition is also accompanied by the formation of a vigorous across-front
94 ageostrophic circulation that can directly influence the production of high-impact weather (e.g.,
95 Winters and Martin 2014, 2016, 2017).

96 Christenson et al. (2017) objectively identified jet superpositions during the cold season
97 (November–March) within the 2.5°-resolution NCEP–NCAR Reanalysis dataset (Kalnay et al.
98 1996; Kistler et al. 2001), and examined the climatological frequency of Northern Hemisphere
99 jet superpositions during 1960–2010. Their analysis indicates that jet superpositions are most
100 frequent in three locations: the western North Pacific, North America, and Northern Africa.
101 Handlos and Martin (2016) provide a detailed examination of the key dynamical processes
102 associated with western North Pacific jet superpositions. These key dynamical processes include
103 equatorward surges of lower-tropospheric cold air over the east Asian continent that strengthen
104 the lower-tropospheric baroclinicity at middle and subtropical latitudes, and the development of
105 widespread convection over the western equatorial Pacific.

106 Prior work concerning North American jet superpositions, however, has focused solely
107 on individual case studies. Winters and Martin (2014, 2016) examined the development of a jet
108 superposition during the 1–3 May 2010 Tennessee Flood, and determined that a substantial
109 fraction of the poleward moisture transport into the southeastern U.S. prior to the second day of
110 the event was accomplished via the across-front ageostrophic circulation associated with the
111 superposed jet. This poleward moisture transport ensured that heavy precipitation continued
112 unabated during the second day of the event. The presence of widespread convection during the
113 2010 Tennessee Flood also contributed to the diabatic erosion of upper-tropospheric potential

114 vorticity (PV) on the equatorward side of the subtropical jet, which facilitated a poleward shift in
115 the position of the subtropical waveguide and the formation of the steep, two-step tropopause
116 structure that accompanied the superposition.

117 Winters and Martin (2016, 2017) performed a complementary analysis of a wintertime jet
118 superposition event at 1200 UTC 20 December 2009 (Fig. 1) that featured a rapidly-deepening
119 surface cyclone beneath the poleward-exit region of the superposed jet. This cyclone was
120 associated with snowfall totals in excess of 30 cm (~1 ft) in locations ranging from the Mid-
121 Atlantic northeastward towards New England. In contrast to the 2010 Tennessee Flood,
122 widespread convection on the equatorward side of the subtropical jet did not play a substantial
123 role in facilitating the development of the superposed jet's two-step tropopause structure in this
124 case. Instead, Winters and Martin (2016, 2017) determined that the descending branch of an
125 across-front ageostrophic circulation within the double-jet environment played the dominant role
126 in restructuring the tropopause prior to superposition.

127 These two cases served as the foundation for the conceptual model of North American jet
128 superpositions (Fig. 2) introduced by Winters and Martin (2017; their Fig. 2). In this model, jet
129 superposition features the development of a polar cyclonic PV anomaly at high latitudes with a
130 polar jet streak located equatorward of the PV anomaly. Polar cyclonic PV anomalies, which
131 include coherent tropopause disturbances (e.g., Hakim 2000; Pyle et al. 2004) and tropopause
132 polar vortices (e.g., Cavallo and Hakim 2009, 2010, 2012, 2013), typify a dynamical
133 environment that can be particularly conducive to surface cyclogenesis at middle and high
134 latitudes (i.e., Hakim et al. 1995, 1996; Pyle et al. 2004; Cavallo and Hakim 2010).

135 Jet superposition also features the concomitant production of a tropical anticyclonic PV
136 anomaly on the equatorward side of the subtropical jet. Tropical anticyclonic PV anomalies

137 result from the poleward transport of tropical, low-PV upper-tropospheric air via tropical plumes,
138 low-latitude troughs, and/or tropical cyclones (e.g., Iskenderian 1995; Roundy et al. 2010;
139 Fröhlich et al. 2013; Archambault et al. 2013, 2015; Winters and Martin 2016). The presence of
140 tropical anticyclonic PV anomalies at midlatitudes typifies a thermodynamic environment
141 characterized by weak upper-tropospheric static stability, and an environment that may feature
142 an atmospheric river (e.g., Newell et al. 1992; Zhu and Newell 1998; Ralph et al. 2004, 2018,
143 2019) within the poleward-directed branch of the anticyclonic PV anomaly's tropospheric-deep
144 circulation.

145 If polar cyclonic and tropical anticyclonic PV anomalies are situated within a confluent
146 large-scale flow pattern and phase favorably, the result is a meridional juxtaposition of the two
147 PV anomalies at midlatitudes. This configuration encourages constructive interference between
148 the nondivergent circulations that accompany each PV anomaly and the rapid acceleration of
149 wind speeds in the area between the two anomalies. The meridional juxtaposition of these two
150 PV anomalies also represents the creation of a dynamical and thermodynamic environment that
151 is particularly conducive to high-impact weather. Once the two PV anomalies are meridionally
152 juxtaposed, mesoscale processes within the near-jet environment, such as across-front
153 ageostrophic circulations (e.g., Shapiro 1981, 1982; Keyser and Pecnick 1985; Keyser and
154 Shapiro 1986; Rotunno et al. 1994; Schultz and Doswell 1999; Schultz and Sanders 2002; Lang
155 and Martin 2012; Martin 2014; Handlos and Martin 2016; Winters and Martin, 2016, 2017) and
156 the diabatic processes that accompany widespread precipitation (e.g., McTaggart-Cowan 2001,
157 2004, 2007; Lee and Kim 2003; Agustí-Panareda et al. 2004; Ahmadi-Givi et al. 2004; Son and
158 Lee 2005; Grams et al. 2011, 2013; Archambault et al. 2013, 2015; Lang and Martin 2013;
159 Grams and Archambault 2016; Handlos and Martin 2016; Winters and Martin 2016, 2017), can

160 act to restructure the tropopause locally to produce the steep, two-step tropopause structure
161 associated with a superposition.

162 While this conceptual model generalizes the process of jet superposition over North
163 America, it does not acknowledge the variable roles that mesoscale processes can play during the
164 production of individual jet superposition events (e.g., Winters and Martin 2016; 2017).
165 Furthermore, the conceptual model in Fig. 2 conceals variability concerning the spectrum of
166 interactions that can occur between polar cyclonic and tropical anticyclonic PV anomalies prior
167 to jet superposition. For instance, an individual jet superposition can arise solely due to a
168 substantial equatorward deviation of the polar jet towards the latitude of the subtropical jet, and
169 vice versa. Therefore, this study adopts a comprehensive approach to examine the multiple
170 “flavors” of North American jet superpositions in greater detail, with the goal of determining the
171 variety of dynamical processes and large-scale evolutions that result in North American jet
172 superpositions.

173 The remainder of this manuscript is structured as follows. Section 2 discusses the
174 objective identification scheme used to identify jet superposition events, as well as the
175 classification scheme employed to partition jet superposition events into characteristic event
176 types. Section 3 discusses the climatological characteristics of each jet superposition event type.
177 Section 4 discusses the composite large-scale flow evolutions associated with the jet
178 superposition event types, and section 5 offers a summary of the most salient results from this
179 study.

180

181 **2. Data and Methodology**

182 This study employs data from the 0.5°-resolution National Centers for Environmental

183 Prediction Climate Forecast System Reanalysis (CFSR; Saha et al. 2010) at 6-h intervals during
184 the period, 1979–2010. This temporal period is chosen to ensure that our analysis period overlaps
185 entirely with the period examined in Christenson et al. (2017), while the CFSR is chosen to
186 obtain a finer resolution of the dynamical evolutions that precede jet superpositions compared to
187 the 2.5°-resolution NCEP–NCAR reanalysis used in prior examinations of superpositions (e.g.,
188 Handlos and Martin 2016; Christenson et al. 2017). All CFSR data were bilinearly interpolated
189 onto isentropic surfaces between 300 K and 380 K at 5-K intervals to accommodate the
190 forthcoming jet superposition identification scheme. This study also utilizes the 2.5°-resolution
191 NOAA Interpolated Outgoing Longwave Radiation (OLR) dataset (Liebmann and Smith 1996)
192 to construct daily composites of OLR for each jet superposition event type. Areas characterized
193 by negative OLR anomalies serve as proxies for the location of extensive cloud cover and may
194 imply the presence of precipitation at midlatitudes if the anomalies overlap with a favorable
195 dynamic and thermodynamic environment for large-scale ascent.

196 *a) Jet Superposition Event Identification*

197 The objective jet superposition identification scheme used in this study is identical to that
198 described in Winters and Martin (2014, 2016), Handlos and Martin (2016), and Christenson et al.
199 (2017). While the forthcoming discussion provides a brief conceptual overview of the
200 identification scheme, the reader is referred to the aforementioned studies for additional detail.

201 The identification of jet superpositions within the CFSR is grid-column based, in that the
202 scheme identifies grid columns that exhibit characteristics of both a polar and a subtropical jet. A
203 polar (subtropical) jet is identified within a grid column if two criteria are satisfied. First, the
204 integrated wind speed within that grid column must exceed 30 m s^{-1} within the 100–400-hPa
205 layer. Second, the magnitude of the horizontal PV gradient within the 1–3-PVU channel at that

206 grid column must exceed an empirically-defined threshold¹ in the 315–330-K (340–355-K)
207 isentropic layer. A strong horizontal PV gradient in the 315–330-K (340–355-K) isentropic layer
208 corresponds to the presence of a “break” between the polar and subtropical tropopauses
209 (subtropical and tropical tropopauses). The identification of a polar and a subtropical jet within
210 the same grid column of CFSR data at a single analysis time results in the identification of a jet
211 superposition within that grid column, and is interpreted physically as the formation of a steep,
212 two-step tropopause structure (e.g., Fig. 1b). On a horizontal map, this scheme is manifest at a
213 single analysis time as a ribbon of positively-identified grid columns that parallel the axis of a
214 superposed jet (not shown).

215 North American jet superpositions were isolated during the cold season (November–
216 March) for this study within a domain bounded in latitude from 10° to 80°N and in longitude
217 from 140°W to 50°W. While jet superpositions do occur outside of the cold season (e.g., the
218 2010 Tennessee Flood), the aforementioned identification scheme would require modifications
219 to account for the vertical movement of the polar and subtropical jet cores throughout the year in
220 order to comprehensively identify jet superpositions during the fall and spring. An effort to
221 investigate the general character of North American jet superpositions during the fall and spring
222 is outside the scope of the present study and is reserved for future work.

223 Following their identification, all 6-h analysis times characterized by a superposition
224 were filtered to retain only those times that rank in the top 10% in terms of the number of grid
225 columns characterized by a jet superposition (≥ 18 grid columns). This filter retains only those
226 situations in which the polar and subtropical jets are superposed for a substantial distance along
227 the jet axis. All grid columns characterized by a jet superposition during a retained analysis time

¹ The specific threshold used for the magnitude of the horizontal PV gradient within the 315–330-K (340–355-K) isentropic layer is 1.4×10^{-5} PVU m^{-1} (0.9×10^{-5} PVU m^{-1}), where $1 \text{ PVU} = 10^{-6} \text{ K m}^2 \text{ kg}^{-1} \text{ s}^{-1}$.

228 were also required to be located within 1000 km of another grid column characterized by a
229 superposition. If an analysis time featured a group of 18 or more grid columns that satisfied this
230 distance criterion, it was labeled a “jet superposition event”. Note that this methodology allows
231 for the identification of multiple jet superposition events at a single analysis time, so long as the
232 groups of jet superposition grid columns are more than 1000 km apart and each group is ≥ 18
233 grid columns in size.

234 The latitude and longitude of each grid column associated with a jet superposition event
235 were averaged to compute a latitude-longitude centroid for that particular event. The positions of
236 the event centroids were then compared across all events to group together jet superposition
237 events that may be associated with the same jet structure. In particular, if an event centroid
238 during one event was located within 1500 km of another event centroid during the previous 30-h
239 period, those jet superposition events were considered to be the same event. The methodology
240 described above produced a total of 326 jet superposition events.

241 *b) Jet Superposition Event Classification*

242 Following their identification, jet superposition events were classified into event types
243 based on the degree to which the polar and subtropical jets deviated from their respective
244 climatological positions to form a superposition. The climatological position of the polar
245 (subtropical) waveguide at a single analysis time (e.g., 0000 UTC 1 January) was calculated by
246 averaging the position of the 2-PVU contour on the 320-K (350-K) isentropic surface at 24-h
247 intervals within a 21-day window centered on that analysis time for every year between 1979 and
248 2010. The 320- and 350-K isentropes reside firmly within the isentropic layers used to identify
249 the polar and subtropical jets, respectively, and serve as reasonable proxies for the positions of

250 the polar and subtropical waveguides during the cold season (e.g., Martius et al. 2010;
251 Christenson et al. 2017).

252 The event classification scheme subsequently compares the position of each jet
253 superposition event centroid against the climatological positions of both the polar and subtropical
254 waveguides at the start of an event. “Polar dominant” events (Fig. 3a) are those events in which
255 an observation of 2 PVU at the location of the event centroid represents a standardized PV
256 anomaly > 0.5 on the 320-K isentropic surface and a standardized PV anomaly > -0.5 on the
257 350-K isentropic surface. Consequently, polar dominant events exhibit a substantial equatorward
258 deviation of the polar jet from its climatological position to superpose with the subtropical jet
259 near its climatological position. “Subtropical dominant” events (Fig. 3c) are those events in
260 which an observation of 2 PVU at the location of the event centroid represents a standardized PV
261 anomaly < 0.5 on the 320-K isentropic surface and a standardized PV anomaly < -0.5 on the
262 350-K isentropic surface. Subtropical dominant events exhibit a substantial poleward deviation
263 of the subtropical jet from its climatological position to superpose with the polar jet near its
264 climatological position. “Hybrid” events (Fig. 3b) are those events in which an observation of 2
265 PVU at the location of the event centroid represents a standardized PV anomaly > 0.5 on the
266 320-K isentropic surface and a standardized PV anomaly < -0.5 on the 350-K isentropic surface.
267 Hybrid events, therefore, exhibit a mutual deviation of the polar and subtropical jets from their
268 respective climatological positions to form a superposition. These categories of jet superposition
269 events represent the spectrum of interactions that can occur between PV anomalies along the
270 polar and subtropical waveguides prior to jet superpositions, and the climatological
271 characteristics of events within these categories will be the focus for the remainder of the study.

272

273 3. Jet Superposition Event Type Characteristics

274 The monthly frequency of North American jet superposition events as a function of event
275 type are shown in Fig. 4. Overall, jet superposition events are most frequent during the months of
276 November and December, and taper off during the remaining months of the cold season. This
277 result is consistent with the findings of Christenson et al. (2017; their Fig. 6), whose analysis
278 shows a broader spatial coverage of North American jet superpositions during November and
279 December compared to January, February, and March. Figure 4 also indicates that subtropical
280 dominant events (N=129) are favored by roughly a 3:2 margin compared to polar dominant
281 events (N=80), suggesting that substantial poleward excursions of the subtropical jet to
282 superpose with the polar jet are more common than the converse evolution. The largest disparity
283 between polar dominant and subtropical dominant events occurs during November and
284 December, when subtropical dominant events are clearly the most frequent event type. Hybrid
285 events (N=117), however, are the most frequent event type during January, February, and March.

286 Figure 5 illustrates the spatial frequency of jet superposition events as a function of event
287 type. Polar dominant events (Fig. 5a) are most frequent along the U.S./Mexico border and along
288 the northern coast of the Gulf of Mexico. The branch of higher frequencies extending towards
289 the northeast U.S. is representative of those polar dominant events that initially develop at low
290 latitudes and propagate downstream within upper-tropospheric southwesterly flow. This
291 evolution is further apparent considering the statistics provided in Table 1. Namely, the average
292 polar dominant event develops at subtropical latitudes (e.g., 29.7°N; 102.0°W). The third and
293 fourth columns of Table 1 reveal the average translation of an individual jet superposition event
294 centroid in latitude-longitude space during its lifespan. A consideration of polar dominant events
295 indicates a northeastward translation in the position of those events throughout their lifespan,

296 consistent with the branch of higher frequencies that extend towards the northeast U.S in Fig. 5a.
297 Hybrid events (Fig. 5b) are most frequent within a 5°-latitude band ranging from 35°N to 40°N,
298 with the largest number of events situated over the southeastern U.S. and western North Atlantic.
299 Hybrid events (34.5°N; 94.3°W) initially develop farther northeast of polar dominant events and
300 translate in a more zonal direction compared to polar dominant events (Table 1).

301 Subtropical dominant events (Fig. 5c) are characterized by two separate frequency
302 maxima centered on the eastern and western coasts of North America, respectively.
303 Consequently, the average location of jet superposition for subtropical dominant events (46.7°N;
304 92.1°W) is not representative of the frequency distribution shown in Fig. 5c. This observation
305 motivated partitioning subtropical dominant events into an “eastern” and “western” category
306 based on the position of each individual event centroid relative to the 96°W meridian at the start
307 of an event. A comparison of the relative frequencies of eastern and western subtropical
308 dominant events shows that eastern events (N=76) are more common than western events
309 (N=53). Furthermore, eastern (48.5°N; 71.2°W) and western (44.0°N; 122.1°W) subtropical
310 dominant events develop at higher latitudes compared to polar dominant and hybrid events, and
311 both subtropical dominant event types translate in a southeastward direction following their
312 development. The latter result suggests that subtropical dominant events often develop at the
313 apex of upper-tropospheric ridges and subsequently propagate downstream within upper-
314 tropospheric northwesterly flow.

315

316 **4. Jet Superposition Event Type Composites**

317 Composite analyses were constructed for each jet superposition event type to examine the
318 synoptic-scale flow evolution during the 48-h period prior to jet superposition. All composites

319 were calculated by shifting the CFSR and OLR data for each event so that each individual event
320 centroid was located at the average starting latitude and longitude for its corresponding event
321 type (Table 1). All CFSR and OLR data were weighted by the cosine of latitude before they were
322 shifted, and a weighted average of the shifted CFSR and OLR data was calculated at each grid
323 point within a domain bounded in latitude from 10°N to 80°N and in longitude from 150°E to
324 10°W to construct the event composites. A two-sided Student's *t*-test was performed on the
325 composite 250-hPa geopotential height, precipitable water, and mean sea level pressure
326 anomalies to identify regions that are statistically distinct from climatology at the 99%
327 confidence level (Wilks 2011). The primary focus of the forthcoming discussion is to determine
328 the dynamical processes that facilitate the development of a steep, two-step tropopause structure
329 during polar, eastern subtropical, and western subtropical dominant superpositions. Hybrid
330 events are not considered further, as the dynamical processes facilitating superposition during
331 those events can be conceptualized as a combination of the processes diagnosed during polar,
332 eastern subtropical, and western subtropical dominant events.

333 *a) Polar Dominant Events*

334 48 h prior to superposition, a surface cyclone is situated in a favorable region for
335 synoptic-scale ascent beneath the poleward-exit region of a zonally-extended and poleward-
336 shifted North Pacific jet stream (Figs. 6a,b). Perturbation upper-tropospheric ridges are located
337 farther downstream over the eastern North Pacific and eastern Canada, respectively, and a
338 perturbation upper-tropospheric trough is positioned over the southwestern U.S. at this time. A
339 weak surface cyclone is in a favorable location for further development downstream of the
340 southwestern U.S. trough and is associated with a zonally-oriented band of negative OLR
341 anomalies. These OLR anomalies are suggestive of increased cloud cover along the developing

342 warm-frontal boundary attendant to the surface cyclone (not shown).

343 The eastern North Pacific ridge amplifies 24 h prior to superposition in conjunction with
344 lower-tropospheric warm-air advection and implied diabatic heating within the warm sector of
345 the surface cyclone in the Gulf of Alaska (Figs. 6c,d). The axis of the eastern North Pacific ridge
346 exhibits a positive tilt at this time, indicating a preference for anticyclonic wave breaking to
347 precede polar dominant superpositions. Anticyclonic wave breaking over the eastern North
348 Pacific subsequently contributes to further amplification of the southwestern U.S. trough 24 h
349 prior to superposition.

350 A maximum in 300-hPa geostrophic warm-air advection is situated downstream of the
351 southwestern U.S. trough 24 h prior to superposition (Fig. 6c), implying that the thermally-
352 indirect circulation within the exit region of the developing superposed jet is shifted equatorward
353 so as to position ascent beneath the jet core (e.g., Shapiro 1981, 1982; Lang and Martin 2012,
354 2013). In response to a favorable environment for synoptic-scale ascent provided by the
355 thermally-indirect circulation within the jet-exit region and the proximity of the southwestern
356 U.S. trough (Figs. 6a,c), the surface cyclone intensifies during the intervening 24-h period (Figs.
357 6b,d). Perturbation southerly geostrophic flow that accompanies the intensified surface cyclone
358 subsequently results in the development of a corridor of anomalous precipitable water within the
359 cyclone's warm sector (Fig. 6d). The collocation of precipitable water anomalies, negative OLR
360 anomalies, and implied ascent within the surface cyclone's warm sector suggests that widespread
361 precipitation accompanies the surface cyclone at this time. Consequently, implied diabatic
362 heating in the vicinity of the surface cyclone likely contributes to an amplification of the
363 downstream ridge over eastern North America by the time of superposition (Fig. 6e).

364 Strengthened 300-hPa geostrophic warm-air advection and enhanced flow curvature

365 downstream of the deep upper-tropospheric trough over the southern Plains at the time of
366 superposition imply that synoptic-scale ascent continues unabated in the vicinity of the surface
367 cyclone during the 24-h period prior to superposition (Figs. 6c,e). As a result, the surface cyclone
368 reaches maximum intensity at the time of superposition (Fig. 6f). Precipitable water anomalies
369 and negative OLR anomalies in the vicinity of the surface cyclone also achieve their maximum
370 magnitudes at this time, suggesting that precipitation maximizes in both intensity and areal
371 coverage concurrently with the formation of a superposition. Any implied areas of precipitation
372 associated with the surface cyclone are located exclusively downstream of the jet superposition
373 event centroid, however (Fig. 6f). Consequently, diabatic processes are located too far
374 downstream to play a direct role in the formation of the two-step tropopause structure that
375 accompanies polar dominant jet superpositions. Diabatic processes do play an *indirect* role in
376 facilitating superposition via their contribution to the amplification of the upper-tropospheric
377 ridge over eastern North America. Namely, downstream flow amplification slows the eastward
378 translation speed of the upper-tropospheric trough over the southern Plains, allowing additional
379 time for the superposition to develop at the base of the trough.

380 Upstream of the jet superposition centroid, the upper-tropospheric flow pattern is
381 characterized by 300-hPa geostrophic cold-air advection that initially develops 24 h prior to
382 superposition (Figs. 6c,e). The presence of geostrophic cold-air advection suggests that the
383 thermally-direct circulation within the jet-entrance region is shifted equatorward so as to position
384 descent beneath the jet core. Labeled the “Shapiro effect” by Rotunno et al. (1994), descent
385 beneath the jet core is strongly conducive to upper-tropospheric frontogenesis and the
386 concomitant development of a tropopause fold (i.e., Shapiro 1981, 1982; Keyser and Pecnick
387 1985; Keyser and Shapiro 1986; Rotunno et al. 1994; Schultz and Doswell 1999; Schultz and

388 Sanders 2002; Lang and Martin 2012; Martin 2014; Winters and Martin 2016, 2017).
389 Consequently, descent beneath the jet-entrance region appears to play a direct role in the
390 formation of the steep, two-step tropopause structure associated with a polar dominant jet
391 superposition.

392 To investigate this assertion more rigorously, a series of cross sections were constructed
393 through the entrance region of the developing superposed jet and perpendicular to the jet axis 12
394 h prior to superposition (B–B') and at the time of superposition (C–C'). Consistent with the
395 presence of 300-hPa geostrophic cold-air advection, these cross sections highlight a region of
396 focused descent beneath and poleward of the jet core 12 h prior to superposition (Fig. 7a) and at
397 the time of jet superposition (Fig. 7b). This descent accounts for a large fraction of the positive
398 PV advection diagnosed along the dynamic tropopause at both times and, consequently, for a
399 downward penetration of high-PV air from the lower stratosphere during the 12-h period prior to
400 superposition (Figs. 7a,b). The downward penetration of high-PV air completes the production of
401 the steep, two-step tropopause structure (Fig. 7b) that must accompany the superposition.

402 The cross sections also highlight the presence of a strong cyclonic PV anomaly on the
403 poleward side of the jet that intensifies in magnitude during the 12-h period prior to
404 superposition (Figs. 7a,b). Notably, the cross sections only highlight a weak anticyclonic PV
405 anomaly above 200 hPa on the equatorward side of the jet. Consequently, the anomalously
406 strong wind speeds that accompany a polar dominant jet superposition are driven
407 disproportionately by the nondivergent circulation that accompanies the strong polar cyclonic PV
408 anomaly. The lack of a strong anticyclonic PV anomaly on the equatorward side of the jet is not
409 surprising, given that this event type requires a superposition to develop at the climatological
410 latitude of the subtropical jet. This result, however, indicates that knowledge of the creation and

411 subsequent transport of polar cyclonic PV anomalies towards subtropical latitudes is essential
412 towards diagnosing the development of a polar dominant jet superposition.

413 *b) Eastern Subtropical Dominant Events*

414 The composite large-scale flow pattern 48 h prior to an eastern subtropical dominant
415 event features a zonally oriented upper-tropospheric trough-ridge couplet centered over eastern
416 North America (Fig. 8a). A surface cyclone is favorably positioned within a region of synoptic-
417 scale ascent immediately downstream of the upper-tropospheric trough and beneath the jet-
418 entrance region, with a surface anticyclone located downstream of the upper-tropospheric ridge
419 over the western North Atlantic (Fig. 8b). The longitudinal juxtaposition of the surface cyclone
420 and anticyclone results in perturbation southerly geostrophic flow over eastern North America
421 and the subsequent poleward transport of anomalous precipitable water into the region. The
422 collocation of precipitable water anomalies and negative OLR anomalies in the vicinity of the
423 surface cyclone's warm-frontal boundary implies that widespread precipitation likely
424 accompanies the surface cyclone at this time. Diabatic heating associated with any implied areas
425 of precipitation subsequently contribute to the observed amplification of the upper-tropospheric
426 ridge over eastern North America during the following 24-h period (Figs. 8a,c).

427 24 h prior to superposition, 300-hPa geostrophic warm-air advection is diagnosed within
428 the entrance region of the developing superposed jet (Fig. 8c). The presence of geostrophic
429 warm-air advection suggests that the thermally-direct circulation within jet-entrance region is
430 shifted poleward relative to the jet axis, positioning ascent directly beneath the jet core at this
431 time (e.g., Shapiro 1981, 1982; Lang and Martin 2012, 2013). Consequently, the surface cyclone
432 remains favorably located within a region of synoptic-scale ascent, which contributed to the
433 intensification of the surface cyclone during the previous 24-h period (Figs. 8b,d). The

434 intensification of both the surface cyclone and the downstream surface anticyclone compared to
435 the prior time results in a strengthened zonal pressure gradient over eastern North America and
436 intensified southerly geostrophic flow (Fig. 8d). This intensified southerly geostrophic flow leads
437 to stronger poleward moisture transport and larger precipitable water anomalies within the
438 surface cyclone's warm sector 24 h prior to superposition. The distribution of negative OLR
439 anomalies at this time overlap the positions of the warm- and cold-frontal boundaries attendant to
440 the surface cyclone (not shown), and the collocation of these OLR anomalies with anomalous
441 moisture and implied ascent suggests that widespread precipitation persists on the equatorward
442 side of the developing superposed jet.

443 The widespread precipitation and implied diabatic heating that accompany the surface
444 cyclone contribute to further amplification of the upper-tropospheric ridge over eastern North
445 America by the time of jet superposition (Figs. 8e,f). Consequently, the subtropical waveguide is
446 displaced anomalously poleward of its climatological position, typical for a subtropical dominant
447 event. While 300-hPa geostrophic warm-air advection persists along the jet axis at the time of
448 superposition, areas of warm-air advection are now focused in the jet-exit rather than in the jet-
449 entrance region, as they were 24 h earlier (Figs. 8c,e). The presence of geostrophic warm-air
450 advection in the jet-exit region suggests that the thermally-indirect circulation within the jet-exit
451 region is shifted equatorward so as to promote continued ascent beneath the jet core (Fig. 8e).
452 While the surface cyclone remains favorably aligned with this area of synoptic-scale ascent, the
453 surface cyclone does not intensify during the 24-h period prior to superposition (Figs. 8d,f).
454 Additionally, precipitable water anomalies and negative OLR anomalies have decreased in
455 magnitude during the intervening 24-h period. Together, these observations imply that surface
456 cyclogenesis and widespread precipitation tend to *lead* the development of eastern subtropical

457 dominant jet superpositions, in contrast to polar dominant events.

458 Farther upstream, 300-hPa geostrophic cold-air advection is diagnosed within the jet-
459 entrance region at the time of jet superposition (Fig. 8e). As discussed during polar dominant
460 events, geostrophic cold-air advection within the jet-entrance region is indicative of descent
461 beneath the jet core. This descent can subsequently act to restructure the tropopause and
462 contribute to the formation of the two-step tropopause structure that accompanies the jet
463 superposition. To investigate the formation of the superposed jet's two-step tropopause structure
464 further, a cross section (D–D') is drawn through the entrance region of the superposed jet and
465 perpendicular to the jet axis. The evolution of the tropopause is investigated within this cross
466 section both 12 h prior to superposition (Fig. 9a) and at the time of superposition (Fig. 9b).

467 Figure 9a depicts an area of ascent directly beneath the jet core 12 h prior to
468 superposition, consistent with the presence of geostrophic warm-air advection along the jet axis
469 and implied ascent along the surface cyclone's attendant frontal boundaries during the 24-h
470 period prior to superposition (Figs. 8c,d). This ascent accounts for a large fraction of the negative
471 PV advection diagnosed along the tropopause and acts to locally steepen the slope of the
472 tropopause during the 12-h period prior to superposition (Figs. 9a,b). Furthermore, given that this
473 ascent is occurring within an anomalously moist environment (Figs. 8d,f), diabatic heating likely
474 contributes to an erosion of upper-tropospheric PV on the equatorward side of the jet (Figs.
475 9a,b). In combination, these two processes reveal the direct role that moist ascent plays during
476 the production of eastern subtropical dominant superpositions through its contribution to the
477 development a tropopause structure that is considerably steeper by the time of superposition. A
478 narrow zone of descent also develops beneath the jet core at the time of superposition (Fig. 9b),
479 in agreement with the geostrophic cold-air advection diagnosed within the jet-entrance region

480 (Fig. 8e). As in polar dominant events, this descent facilitates the downward transport high-PV
481 air from the lower stratosphere and contributes to the depth of the resultant two-step tropopause
482 structure that defines the jet superposition.

483 In contrast to polar dominant events (Figs. 7a,b), the cross sections shown in Figs. 9a,b
484 indicate that the superposed jet is characterized by the horizontal juxtaposition of a polar
485 cyclonic and a tropical anticyclonic PV anomaly during the 12-h period prior to superposition.
486 This configuration of upper-tropospheric PV anomalies strongly resembles the conceptual model
487 shown within Fig. 2 and indicates that the nondivergent circulations that accompany each PV
488 anomaly add constructively to produce the anomalously strong wind speeds associated with
489 eastern subtropical dominant jet superpositions. Consequently, knowledge of the creation,
490 transport towards midlatitudes, and phasing of these two PV anomalies is critical towards
491 diagnosing the development of this jet superposition event type.

492 *c) Western Subtropical Dominant Events*

493 The development of western subtropical dominant events features the meridional
494 juxtaposition of an anomalous upper-tropospheric trough at high latitudes and an anomalous
495 ridge at subtropical latitudes 48 h prior to superposition, which results in a zonal extension of the
496 North Pacific jet stream (Fig. 10a). A surface cyclone is situated beneath the poleward-exit
497 region of the jet, and is characterized by a corridor of anomalous precipitable water within
498 perturbation southwesterly geostrophic flow on the cyclone's equatorward flank (Fig. 10b). The
499 aspect ratio of this corridor of anomalous precipitable water strongly resembles the character of
500 landfalling western U.S. atmospheric rivers (e.g., Newell et al. 1992; Zhu and Newell, 1998;
501 Ralph et al. 2004, 2018, 2019; Cannon et al. 2018), and is collocated with broad regions of 300-
502 hPa geostrophic warm-air advection and negative OLR anomalies. Consequently, the thermally-

503 indirect circulation within the jet-exit region favors synoptic-scale ascent and the production of
504 precipitation beneath the jet core in the vicinity of the Pacific Northwest at this time.
505 Perturbation geostrophic winds near the surface are also oriented perpendicular to the west coast
506 of North America, which suggests that orographic ascent likely contributes to the production of
507 precipitation during these events, as well.

508 Diabatic heating that accompanies any areas of implied ascent is primarily confined
509 equatorward of the developing superposed jet, suggesting that diabatic heating contributes to the
510 amplification of the eastern North Pacific ridge 24 h prior to superposition (Fig. 10c). The upper-
511 tropospheric trough poleward of the developing superposed jet also amplifies compared to the
512 prior time, which leads to the acceleration of a jet streak west of the North American continent.
513 The surface cyclone intensifies compared to the prior time beneath the poleward-exit region of
514 the developing superposed jet, and is characterized by a stronger and more spatially-coherent
515 corridor of anomalous precipitable water on its equatorward flank (Fig. 10d). The intersection of
516 anomalous precipitable water with negative OLR anomalies, stronger 300-hPa geostrophic
517 warm-air advection, and onshore lower-tropospheric geostrophic flow (Figs. 10c,d) suggests that
518 widespread precipitation persists along the west coast of North America on the equatorward side
519 of the developing superposed jet 24 h prior to superposition.

520 The perturbation upper-tropospheric trough and ridge near the west coast of North
521 America achieve their maximum intensity at the time of jet superposition, resulting in further
522 acceleration of the wind speeds along the axis of the now superposed jet (Fig. 10e). The surface
523 cyclone remains within a favorable environment for synoptic-scale ascent beneath the poleward-
524 exit region of the superposed jet, with its corridor of anomalous precipitable water focused
525 farther south than at prior times along the central California coast (Figs. 10e,f). Negative OLR

526 anomalies and sea level pressure anomalies decrease in magnitude, however, during the 24-h
527 period prior to superposition (Figs. 10d,f). As in eastern subtropical dominant events, this
528 observation suggests that surface cyclogenesis and widespread precipitation *lead* the formation
529 of western subtropical dominant events.

530 As in polar and eastern subtropical dominant events, 300-hPa geostrophic cold-air
531 advection develops within the entrance region of the jet at the time of superposition (Fig. 10e),
532 indicating that the thermally-direct circulation in that location focuses descent beneath the jet
533 core. To examine the impact of this descent as well as implied diabatic processes on the
534 production of the jet's two-step tropopause structure, a cross section (E–E') is constructed
535 through the entrance region of the superposed jet and perpendicular to the jet axis. Figure 11a
536 demonstrates that a focused region of ascent is present beneath the developing jet superposition
537 12 h prior to superposition, consistent with the presence of geostrophic warm-air advection along
538 a considerable portion of the jet axis prior to superposition (Figs. 10c,e). This ascent accounts for
539 a large fraction of the negative PV advection diagnosed along the tropopause and acts to locally
540 steepen the tropopause. Additionally, given that this ascent is occurring within a corridor of
541 anomalous moisture, diabatic heating that accompanies the ascent likely contributes to an erosion
542 of upper-tropospheric PV on the equatorward side of the jet during the 12-h period prior
543 superposition (Figs. 11a,b). The erosion of upper-tropospheric PV subsequently acts to further
544 steepen the tropopause by the time of superposition.

545 A narrow zone of descent is diagnosed directly beneath the superposed jet core at the
546 time of superposition (Fig. 11b). As in the previous event composites, this descent accounts for
547 positive PV advection at the base of the tropopause break and, consequently, a downward
548 penetration of high-PV air from the lower stratosphere. The downward transport of high-PV air

549 from the lower stratosphere further steepens the tropopause and contributes to the formation of
550 the two-step tropopause structure that prevails at the time of superposition. Both cross sections
551 shown in Figs. 11a,b also demonstrate that the superposed jet is characterized by the meridional
552 juxtaposition of a polar cyclonic and tropical anticyclonic PV anomaly near the tropopause.
553 Consequently, the acceleration of wind speeds in the vicinity of the superposition results from
554 the constructive interference between the nondivergent circulations that accompany each PV
555 anomaly. Therefore, as in eastern subtropical dominant events, knowledge of the creation,
556 transport towards midlatitudes, and phasing of these two PV anomalies is critical for diagnosing
557 the production of a western subtropical dominant event.

558

559 **5. Conclusion**

560 This study classifies North American jet superposition events into characteristic event
561 types based on the relative deviation of the polar and subtropical jets from their respective
562 climatological latitude bands, and investigates the dynamical mechanisms that facilitate the
563 production of a steep, two-step tropopause structure during each jet superposition event type.
564 The dynamical evolutions associated with each jet superposition event type are summarized
565 through a series of conceptual models presented in Fig. 12.

566 Polar dominant events (Fig. 12a) exhibit a preference for anticyclonic wave breaking
567 over the eastern North Pacific during the 48-h period prior to jet superposition. Anticyclonic
568 wave breaking subsequently facilitates the equatorward transport of a polar cyclonic PV anomaly
569 towards subtropical latitudes and allows the polar jet to superpose with the subtropical jet near
570 the climatological position of the subtropical jet. Surface cyclogenesis occurs within the
571 poleward-exit region of the jet and peaks in intensity concurrently with the development of the

572 superposition. The surface cyclone features anomalous poleward moisture transport within its
573 warm sector, and is likely associated with widespread precipitation that also peaks in intensity
574 and spatial coverage at the time of superposition. Given that surface cyclogenesis and areas of
575 implied precipitation are located downstream of the jet superposition, moist ascent and diabatic
576 heating do not play a direct role in the formation of the two-step tropopause structure that
577 accompanies polar dominant events. Instead, upper-tropospheric geostrophic cold-air advection
578 within the entrance region of the developing superposed jet is indicative of descent beneath the
579 jet core. This descent is determined to play the primary role in facilitating the development of the
580 superposed jet's two-step tropopause structure during polar dominant events.

581 In contrast to polar dominant events, surface cyclogenesis and implied precipitation *lead*
582 the development of eastern subtropical dominant events (Fig. 12b). In particular, surface
583 cyclogenesis and implied precipitation occur predominantly within the equatorward-entrance
584 region of the developing superposed jet. Moist ascent, therefore, plays a direct role in the
585 development of the superposed jet's two-step tropopause structure by locally steepening the
586 tropopause via tilting and via the diabatic erosion of upper-tropospheric PV on the equatorward
587 side of the jet. As in polar dominant events, upper-tropospheric geostrophic cold-air advection
588 develops within the jet-entrance region during the 24-h period immediately preceding
589 superposition and indicates descent beneath the jet core in that location. This descent acts to
590 steepen the tropopause further by the time of superposition via the subduction of high-PV air
591 from the lower stratosphere, thereby completing the formation of the superposed jet's two-step
592 tropopause structure.

593 Western subtropical dominant events (Fig. 12c) are characterized by surface cyclogenesis
594 that occurs beneath the poleward-exit region of the jet, rather than beneath the equatorward jet-

595 entrance region as observed during eastern subtropical dominant events. The surface cyclone is
596 accompanied by a zonally-oriented corridor of anomalous moisture that strongly resembles the
597 character of a western U.S. atmospheric river. Widespread ascent and implied precipitation
598 diagnosed along this corridor of anomalous moisture peak *prior* to the development of jet
599 superposition, as in eastern subtropical events, and play a direct role in the production of the
600 superposed jet's two-step tropopause structure by steepening the tropopause locally via tilting
601 and via the diabatic erosion of upper-tropospheric PV on the equatorward side of the jet. As
602 observed during the other event types, upper-tropospheric geostrophic cold-air advection
603 develops within the jet-entrance region by the time of superposition. Consequently, descent plays
604 a critical role in completing the production of western subtropical dominant jet superpositions by
605 contributing to the production of the superposed jet's two-step tropopause structure, as well.

606 The event types considered as part of this study reveal the varied roles that diabatic
607 processes can play during the production of North American jet superpositions. Namely, surface
608 cyclogenesis and implied precipitation contribute directly to the formation of a two-step
609 tropopause structure during subtropical dominant events, whereas surface cyclogenesis and
610 implied precipitation develop concurrently with and downstream of polar dominant events. This
611 difference motivates additional work investigating the relative importance of diabatic processes
612 during observed jet superposition events. Of particular interest, is whether the omission of
613 diabatic processes during the 48-h period prior to each jet superposition event type results in the
614 successful formation of a jet superposition. It is hypothesized that subtropical dominant events
615 are more sensitive to the omission of diabatic processes than polar dominant events, given the
616 direct role that diabatic processes appear to play in restructuring the tropopause during that event
617 type. The scrutiny of dry and full-physics simulations for select jet superposition events within

618 each event type is one pathway through which to examine the role that diabatic processes play
619 during jet superpositions in greater detail.

620 A key result from this study is that descent beneath the entrance region of a developing
621 jet superposition is a shared element regardless of the event type under consideration. This result
622 motivates two critical research questions concerning the production of descent during jet
623 superposition events. First, what fraction of the observed descent is due to across-front
624 ageostrophic circulations that arise due to geostrophic frontogenesis within the confluent jet-
625 entrance region (i.e., divergence of the across-front component of the \mathbf{Q} -vector) versus along-
626 front couplets of vertical motion that arise due to flow curvature and are of the scale of baroclinic
627 waves (i.e., divergence of the along-front component of the \mathbf{Q} -vector; e.g., Keyser et al. 1992;
628 Martin 2006; Martin 2014)? The large-scale evolutions discussed in section 4 demonstrate that
629 both of these processes are certain to operate within North American jet superposition
630 environments. Second, what fraction of the observed descent within each event type can be
631 attributed to the three-dimensional circulations that accompany upper-tropospheric PV anomalies
632 along the polar and subtropical waveguides? The answer to the second question, in particular, is
633 likely to reveal the relative influence that polar cyclonic and tropical anticyclonic PV anomalies
634 have on the production of a superposed jet's two-step tropopause structure during each event
635 type.

636 North American jet superposition events during the cool season are most frequent during
637 November and December, rather than during January and February as they are in the western
638 North Pacific and northern Africa (Christenson et al. 2017; their Fig. 6). Given that North
639 American jet superpositions are generally preceded by the development of a high-amplitude flow
640 pattern, the frequency distribution of North American jet superposition events throughout the

641 cold season may be related to the lower frequency of Rossby wave breaking events in the eastern
642 North Pacific during the winter compared to the fall and spring (e.g., Abatzoglou and
643 Magnusdottir 2006; Bowley et al. 2019). Additionally, prior case study work suggests that jet
644 superpositions can form outside of the cold season (i.e., Christenson 2013; Winters and Martin
645 2014, 2016). Therefore, subsequent examinations of jet superposition events should modify the
646 jet identification scheme employed within this study to identify superposition events during the
647 fall and spring. A comparison between jet superposition events across seasons has the potential
648 to highlight the degree to which the dynamical processes and the types of sensible weather
649 impacts that accompany jet superposition events vary as a function of season.

650 The composite analyses investigated in this study demonstrate that jet superpositions are
651 often associated with surface cyclogenesis, and a dynamical and thermodynamic environment
652 that is conducive to the production of widespread precipitation. However, a cursory examination
653 of individual events within each jet superposition event type indicates that some events are not
654 necessarily associated with sensible weather within the near-jet environment that can be
655 characterized as “high-impact”. Consequently, future work that compares jet superposition
656 environments that lead to high-impact weather events versus those that result in null events
657 offers the potential provide benefits to operational forecasts of high-impact weather. Finally, the
658 development and subsequent downstream propagation superposed jets can strongly reconfigure
659 the large-scale flow pattern over the North Atlantic. Consequently, further understanding of the
660 impacts that North American jet superpositions may have on the downstream large-scale flow
661 pattern may offer important implications for operational forecasts of conditions in western
662 Europe.

663

664 *Acknowledgments*

665 This work was supported by the National Science Foundation through an AGS Postdoctoral
666 Research Fellowship (AGS-1624316) held at the University at Albany, SUNY by ACW.

667 **References**

- 668 Abatzoglou, J. T., and G. Magnusdottir, 2006: Planetary wave breaking and nonlinear reflection:
669 Seasonal cycle and interannual variability. *J. Climate*, **19**, 6139–6152,
670 doi: 10.1175/JCLI3968.1.
- 671 Agustí-Panareda, A., C. D. Thorncroft, G. C. Craig, and S. L. Gray, 2004: The extratropical
672 transition of Hurricane Irene (1999): A potential-vorticity perspective. *Quart. J. Roy.*
673 *Meteor. Soc.*, **130**, 1047–1074, doi: 10.1256/qj.02.140.
- 674 Ahmadi-Givi, F., G. C. Craig, and R. S. Plant, 2004: The dynamics of a midlatitude cyclone with
675 very strong latent-heat release. *Quart. J. Roy. Meteor. Soc.*, **130**, 295–323, doi:
676 10.1256/qj.02.226.
- 677 Archambault, H. M., L. F. Bosart, D. Keyser, and J. M. Cordeira, 2013: A climatological
678 analysis of the extratropical flow response to recurving western North Pacific tropical
679 cyclones. *Mon. Wea. Rev.*, **141**, 2325–2346, doi: 10.1175/MWR-D-12-00257.1.
- 680 Archambault, H. M., D. Keyser, L. F. Bosart, C. A. Davis, and J. M. Cordeira, 2015: A
681 composite perspective of the extratropical flow response to recurving western North
682 Pacific tropical cyclones. *Mon. Wea. Rev.*, **143**, 1122–1141, doi: 10.1175/MWR-D-14-
683 00270.1.
- 684 Bowley, K. A., J. R. Gyakum, and E. H. Atallah, 2019: A new perspective toward cataloging
685 Northern Hemisphere Rossby wave breaking on the dynamic tropopause. *Mon. Wea.*
686 *Rev.*, **147**, 409–431, doi: 10.1175/MWR-D-18-0131.1.
- 687 Cannon, F., C. W. Hecht, J. M. Cordeira, and F. M. Ralph, 2018: Synoptic and mesoscale forcing
688 of southern California extreme precipitation. *J. Geophys. Res.: Atmospheres*, **123**, 13714–
689 13730, doi: 10.1029/2018JD029045.

690 Cavallo, S. M., and G. J. Hakim, 2009: Potential vorticity diagnosis of a tropopause polar
691 cyclone. *Mon. Wea. Rev.*, **137**, 1358–1371, doi: 10.1175/2008MWR2670.1.

692 Cavallo, S. M., and G. J. Hakim, 2010: Composite structure of tropopause polar cyclones. *Mon.*
693 *Wea. Rev.*, **138**, 3840–3857, doi: 10.1175/2010MWR3371.1.

694 Cavallo, S. M., and G. J. Hakim, 2012: Radiative impact on tropopause polar vortices over the
695 Arctic. *Mon. Wea. Rev.*, **140**, 1683–1702, doi: 10.1175/MWR-D-11-00182.1.

696 Cavallo, S. M., and G. J. Hakim, 2013: Physical mechanisms of tropopause polar vortex intensity
697 change. *J. Atmos. Sci.*, **70**, 3359–3373, doi: 10.1175/JAS-D-13-088.1.

698 Christenson, C. E., 2013: A synoptic-climatology of Northern Hemisphere polar and subtropical
699 jet superposition events. M.S. thesis, University of Wisconsin–Madison, 62 pp.

700 Christenson, C. E., J. E. Martin, Z. J. Handlos, 2017: A synoptic climatology of Northern
701 Hemisphere, cold season polar and subtropical jet superposition events. *J. Climate*, **30**,
702 7231–7246, doi: 10.1175/JCLI-D-16-0565.1.

703 Defant, F., and H. Taba, 1957: The threefold structure of the atmosphere and the characteristics
704 of the tropopause. *Tellus*, **9**, 259–275, doi:10.3402/tellusa.v9i3.9112.

705 Fröhlich, L., P. Knippertz, A. H. Fink, and E. Hohberger, 2013: An objective climatology of
706 tropical plumes. *J. Climate*, **26**, 5044–5060, doi: 10.1175/JCLI-D-12-00351.1.

707 Grams, C. M., H. Wernli, M. Böttcher, J. Čampa, U. Corsmeier, S. C. Jones, J. H. Keller, C.-J.
708 Lenz, and L. Wiegand, 2011: The key role of diabatic processes in modifying the upper-
709 tropospheric wave guide: A North Atlantic case-study. *Quart. J. Roy. Meteor. Soc.*, **137**,
710 2174–2193, doi: 10.1002/qj.891.

711 Grams, C. M., S. C. Jones, C. A. Davis, P. A. Harr, and M. Weissmann, 2013: The impact of
712 Typhoon Jangmi (2008) on the midlatitude flow. Part I: Upper-level ridgebuilding and

713 modification of the jet. *Quart. J. Roy. Meteor. Soc.*, **139**, 2148–2164, doi:
714 10.1002/qj.2091.

715 Grams, C. M., H. M. Archambault, 2016: The key role of diabatic outflow in amplifying the
716 midlatitude flow: A representative case study of weather systems surrounding western
717 North Pacific extratropical transition. *Mon. Wea. Rev.*, **144**, 3847–3869, doi:
718 10.1175/MWR-D-15-0419.1.

719 Hakim, G. J., 2000: Climatology of coherent structures on the extratropical tropopause. *Mon.*
720 *Wea. Rev.*, **128**, 385–406, doi: 10.1175/1520-
721 0493%282000%29128<0385%3ACOCSOT>2.0.CO%3B2.

722 Hakim, G. J., L. F. Bosart, and D. Keyser, 1995: The Ohio Valley wave-merger cyclogenesis
723 event of 25–26 January 1978. Part I: Multiscale case study. *Mon. Wea. Rev.*, **123**, 2663–
724 2692, doi: 10.1175/1520-0493(1995)123<2663:TOVWMC>2.0.CO;2.

725 Hakim, G. J., D. Keyser, and L. F. Bosart, 1996: The Ohio Valley wave-merger cyclogenesis
726 event of 25–26 January 1978. Part II: Diagnosis using quasigeostrophic potential vorticity
727 inversion. *Mon. Wea. Rev.*, **124**, 2176–2205, doi: 10.1175/1520-
728 0493(1996)124<2176:TOVWMC>2.0.CO;2.

729 Handlos, Z. J., and J. E. Martin, 2016: Composite analysis of large-scale environments
730 conducive to west Pacific polar/subtropical jet superposition. *J. Climate*, **29**, 7145–7165,
731 doi: 10.1175/JCLI-D-16-0044.1.

732 Held, I. M., 1975: Momentum transport by quasi-geostrophic eddies. *J. Atmos. Sci.*, **32**, 1494–
733 1497, doi: 10.1175/1520-0469(1975)032,1494:MTBQGE.2.0.CO;2.

734 Held, I. M., and A. Y. Hou, 1980: Nonlinear axially symmetric circulations in a nearly inviscid
735 atmosphere. *J. Atmos. Sci.*, **37**, 515–533, doi: 10.1175/1520-
736 0469(1980)037<0515:NASCIA>2.0.CO;2.

737 Iskenderian, H., 1995: A 10-year climatology of Northern Hemisphere tropical cloud plumes and
738 their composite flow patterns. *J. Climate*, **8**, 1630–1637, doi: 10.1175/1520-
739 0442(1995)008<1630:AYCONH>2.0.CO;2.

740 Kalnay, E., and Coauthors, 1996: The NCEP/NCAR 40-Year Reanalysis Project. *Bull. Amer.*
741 *Meteor. Soc.*, **77**, 437–470, doi: 10.1175/1520-0477(1996)077,0437:TNYRP.2.0.CO;2.

742 Keyser, D., and M. J. Pecnick, 1985: A two-dimensional primitive equation model of
743 frontogenesis forced by confluence and horizontal shear. *J. Atmos. Sci.*, **42**, 1259–1282,
744 doi: 10.1175/1520-0469(1985)042,1259:ATDPEM.2.0.CO;2.

745 Keyser, D., and M. A. Shapiro, 1986: A review of the structure and dynamics of upper-level
746 frontal zones. *Mon. Wea. Rev.*, **114**, 452–499, doi: 10.1175/1520-
747 0493(1986)114<0452:AROTSA>2.0.CO;2.

748 Keyser, D., B. D. Schmidt, and D. G. Duffy, 1992: Quasigeostrophic vertical motions diagnosed
749 from along- and cross-isentrope components of the Q vector. *Mon. Wea. Rev.*, **120**, 731–
750 741, doi: 10.1175/1520-0493%281992%29120<0731%3AQVMDFA>2.0.CO%3B2.

751 Kistler, R., and Coauthors, 2001: The NCEP–NCAR 50-Year Reanalysis: Monthly means CD-
752 ROM and documentation. *Bull. Amer. Meteor. Soc.*, **82**, 247–267, doi: 10.1175/ 1520-
753 0477(2001)082,0247:TNNYRM.2.3.CO;2.

754 Koteswaram, P., 1953: An analysis of the high tropospheric wind circulation over India in
755 winter. *Indian J. Meteor. Geophys.*, **4**, 13–21.

756 Koteswaram, P., and S. Parthasarathy, 1954: The mean jet stream over Indian in the pre-
757 monsoon and post-monsoon seasons and vertical motions associated with subtropical jet
758 streams. *Indian J. Meteor. Geophys.*, **5**, 138–156.

759 Krishnamurti, T. N., 1961: The subtropical jet stream of winter. *J. Meteor.*, **18**, 172–191, doi:
760 10.1175/1520-0469(1961)018<0172:TSJSOW>2.0.CO;2.

761 Lang, A. A., and J. E. Martin, 2012: The structure and evolution of lower stratospheric frontal
762 zones. Part I: Examples in northwesterly and southwesterly flow. *Quart. J. Roy. Meteor.*
763 *Soc.*, **138**, 1350–1365, doi: 10.1002/qj.843.

764 Lang, A. A., and J. E. Martin, 2013: The structure and evolution of lower stratospheric frontal
765 zones: Part II: The influence of tropospheric ascent on lower stratospheric frontal
766 development. *Quart. J. Roy. Meteor. Soc.*, **139**, 1798–1809, doi: 10.1002/qj.2074.

767 Lee, S., and H.-K. Kim, 2003: The dynamical relationship between subtropical and eddy-driven
768 jets. *J. Atmos. Sci.*, **60**, 1490–1503, doi: 10.1175/1520-
769 0469%282003%29060<1490%3ATDRBSA>2.0.CO%3B2.

770 Liebmann, B., and C. A. Smith, 1996: Description of a complete (interpolated) outgoing
771 longwave radiation dataset. *Bull. Amer. Meteor. Soc.*, **77**, 1275–1277.

772 Loewe, F., and V. Radok, 1950: A meridional aerological cross section in the southwest
773 Pacific. *J. Meteor.*, **7**, 58–65, doi: 10.1175/1520-
774 0469(1950)007<0058:AMACSI>2.0.CO;2.

775 Martin J. E., 2006. The role of shearwise and transverse quasigeostrophic vertical motions in the
776 midlatitude cyclone life cycle. *Mon. Wea. Rev.*, **134**, 1174–1193, doi:
777 10.1175/MWR3114.1.

778 Martin, J. E., 2014: Quasi-geostrophic diagnosis of the influence of vorticity advection on the
779 development of upper level jet-front systems. *Quart. J. Roy. Meteor. Soc.*, **140**, 2658–
780 2671, doi: 10.1002/qj.2333.

781 Martius, O., C. Schwiertz, and H. C. Davies, 2010: Tropopause-level waveguides. *J. Atmos.*
782 *Sci.*, **67**, 866–879, doi: 10.1175/2009JAS2995.1.

783 McTaggart-Cowan, R., J. R. Gyakum, and M. K. Yau, 2001: Sensitivity testing of extratropical
784 transitions using potential vorticity inversions to modify initial conditions: Hurricane Earl
785 case study. *Mon. Wea. Rev.*, **129**, 1617–1636, doi: 10.1175/1520-
786 0493%282001%29129<1617%3ASTOETU>2.0.CO%3B2.

787 McTaggart-Cowan, R., J. R. Gyakum, and M. K. Yau, 2004: The impact of tropical remnants on
788 extratropical cyclogenesis: Case study of Hurricanes Danielle and Earl (1998). *Mon.*
789 *Wea. Rev.*, **132**, 1933–1951, doi: 10.1175/1520-
790 0493%282004%29132<1933%3ATIOTRO>2.0.CO%3B2.

791 McTaggart-Cowan, R., L. F. Bosart, J. R. Gyakum, and E. H. Atallah, 2007: Hurricane Katrina
792 (2005). Part II: Evolution and hemispheric impacts of a diabatically generated warm pool.
793 *Mon. Wea. Rev.*, **135**, 3927–3949, doi: 10.1175/2007MWR2096.1.

794 McWilliams, J. C., and J. H. S. Chow, 1981: Equilibrium geostrophic turbulence I: Reference
795 solution in a b-plane channel. *J. Phys. Oceanogr.*, **11**, 921–949, doi: 10.1175/1520-
796 0485(1981)011,0921:EGTIAR.2.0.CO;2.

797 Mohri, K., 1953: On the fields of wind and temperature over Japan and adjacent waters during
798 winter of 1950–1951. *Tellus*, **5**, 340–358, doi: 10.3402/tellusa.v5i3.8582.

799 Namias, J., and P. F. Clapp, 1949: Confluence theory of the high tropospheric jet stream. *J.*
800 *Meteor.*, **6**, 330–336, doi: 10.1175/1520-0469(1949)006<0330:CTOTHT>2.0.CO;2.

801 Newell, R. E., N. E. Newell, Y. Zhu, and C. Scott, 1992: Tropospheric rivers?—A pilot
802 study. *Geophys. Res. Lett.*, **19**, 2401–2404, doi: 10.1029/92GL02916.

803 Newton, C. W., 1954: Frontogenesis and frontolysis as a three-dimensional process. *J.*
804 *Meteor.*, **11**, 449–461, doi: 10.1175/1520-0469(1954)011<0449:FAFAAT>2.0.CO;2.

805 Palmén, E., and C. W. Newton, 1948: A study of the mean wind and temperature distribution in
806 the vicinity of the polar front in winter. *J. Meteor.*, **5**, 220–226, doi: 10.1175/1520-
807 0469(1948)005<0220:ASOTMW>2.0.CO;2.

808 Palmén, E., and C. W. Newton, 1969: *Atmospheric Circulation Systems: Their Structure and*
809 *Physical Interpretation*. Academic Press, 603 pp.

810 Panetta, R. L., 1993: Zonal jets in wide baroclinically unstable regions: Persistence and scale
811 selection. *J. Atmos. Sci.*, **50**, 2073–2106, doi: 10.1175/1520-
812 0469(1993)050,2073:ZJIWBU.2.0.CO;2.

813 Pyle, M. E., D. Keyser, and L. F. Bosart, 2004: A diagnostic study of jet streaks: Kinematic
814 signatures and relationship to coherent tropopause disturbances. *Mon. Wea.*
815 *Rev.*, **132**, 297–319, doi: 10.1175/1520-0493(2004)132<0297:ADSOJS>2.0.CO;2.

816 Ralph, F. M., P. J. Neiman, and G. A. Wick, 2004: Satellite and CALJET aircraft observations of
817 atmospheric rivers over the eastern North Pacific Ocean during the winter of
818 1997/98. *Mon. Wea. Rev.*, **132**, 1721–1745, doi: 10.1175/1520-
819 0493(2004)132<1721:SACAOO>2.0.CO;2.

820 Ralph, F. M., M. D. Dettinger, M. M. Cairns, T. J. Galarneau, and J. Eylander, 2018: Defining
821 “atmospheric river”: How the *Glossary of Meteorology* helped resolve a debate. *Bull.*
822 *Amer. Meteor. Soc.*, **99**, 837–839, doi: 10.1175/BAMS-D-17-0157.1

823 Ralph, F. M., and Coauthors, 2019: A scale to characterize the strength of impacts of
824 atmospheric rivers. *Bull. Amer. Meteor. Soc.*, **100**, 269–289, doi: 10.1175/BAMS-D-18-
825 0023.1.

826 Rhines, P. B., 1975: Waves and turbulence on a beta-plane. *J. Fluid Mech.*, **69**, 417–433, doi:
827 10.1017/S0022112075001504.

828 Riehl, H., 1962: Jet streams of the atmosphere. Dept. of Atmospheric Science Tech. Rep. 32,
829 Colorado State University, Fort Collins, CO, 117 pp.

830 Rotunno, R., W. C. Skamarock, and C. Snyder, 1994: An analysis of frontogenesis in numerical
831 simulations of baroclinic waves. *J. Atmos. Sci.*, **51**, 3373–3398, doi: 10.1175/1520-
832 0469(1994)051,3373:AAOFIN.2.0.CO;2

833 Roundy, P. E., K. MacRitchie, J. Asuma, and T. Melino, 2010: Modulation of the global
834 atmospheric circulation by combined activity in the Madden–Julian oscillation and the El
835 Niño–Southern Oscillation during boreal winter. *J. Climate*, **23**, 4045–4059, doi:
836 10.1175/2010JCLI3446.1.

837 Saha, S., and Coauthors, 2010: The NCEP Climate Forecast System Reanalysis. *Bull. Amer.*
838 *Meteor. Soc.*, **91**, 1015–1057, doi: 10.1175/2010BAMS3001.1.

839 Schultz, D. M., and C. A. Doswell III, 1999: Conceptual models of upperlevel frontogenesis in
840 south-westerly and north-westerly flow. *Quart. J. Roy. Meteor. Soc.*, **125**, 2535–2562,
841 doi: 10.1002/qj.49712555910.

842 Schultz, D. M., and F. Sanders, 2002: Upper-level frontogenesis associated with the birth of
843 mobile troughs in northwesterly flow. *Mon. Wea. Rev.*, **130**, 2593–2610, doi:
844 10.1175/1520-0493 (2002)130,2593:ULFAWT.2.0.CO;2.

845 Shapiro, M. A., 1981: Frontogenesis and geostrophically forced secondary circulations in the
846 vicinity of jet stream-frontal zone systems. *J. Atmos. Sci.*, **38**, 954–973, doi:
847 10.1175/1520-0469(1981)038<0954:FAGFSC>2.0.CO;2.

848 Shapiro, M. A., 1982: *Mesoscale weather systems of the central United States*. CIRES, 78 pp.

849 Shapiro, M. A., T. Hampel, and A. J. Krueger, 1987: The Arctic tropopause fold. *Mon. Wea.*
850 *Rev.*, **115**, 444–454, doi: 10.1175/1520-0493(1987)115,0444:TATF.2.0.CO;2.

851 Shapiro, M. A., and D. Keyser, 1990: Fronts, jet streams, and the tropopause. *Extratropical*
852 *Cyclones: The Erik Palmén Memorial Volume*, C. Newton and E. O. Holopainen, Eds.,
853 Amer. Meteor. Soc., 167–191.

854 Son, S.-W., and S. Lee, 2005: The response of westerly jets to thermal driving in a primitive
855 equation model. *J. Atmos. Sci.*, **62**, 3741–3757, doi: 10.1175/JAS3571.1.

856 Sutcliffe, R. C., and J. K. Bannon, 1954: Seasonal changes in the upper-air conditions in the
857 Mediterranean Middle East area. *Proc. Int. Association of Meteorology*, Rome, Italy, Int.
858 Union of Geodesy and Geophysics. 322–334.

859 Wilks, D. S., 2011: *Statistical Methods in the Atmospheric Sciences*. 3rd ed. Elsevier, 676 pp.

860 Winters, A. C., and J. E. Martin, 2014: The role of a polar/subtropical jet superposition in the
861 May 2010 Nashville flood. *Wea. Forecasting*, **29**, 954–974, doi: 10.1175/WAF-D-13-
862 00124.1.

863 Winters, A. C., and J. E. Martin, 2016: Synoptic and mesoscale processes supporting vertical
864 superposition of the polar and subtropical jets in two contrasting cases. *Quart. J. Roy.*
865 *Meteor. Soc.*, **142**, 1133–1149, doi: 10.1002/qj.2718.

866 Winters, A. C., and J. E. Martin, 2017: Diagnosis of a North American polar–subtropical jet
867 superposition employing piecewise potential vorticity inversion. *Mon. Wea.*
868 *Rev.*, **145**, 1853–1873, doi: 10.1175/MWR-D-16-0262.1.

869 Yeh, T. C., 1950: The circulation of the high tropopause over China in the winter of 1945–
870 46. *Tellus*, **2**, 173–183, doi: 10.3402/tellusa.v2i3.8548.

871 Zhu, Y., and R. E. Newell, 1998: A proposed algorithm for moisture fluxes from atmospheric
872 rivers. *Mon. Wea. Rev.*, **126**, 725–735, doi: 10.1175/1520-
873 0493(1998)126<0725:APAFMF>2.0.CO;2.

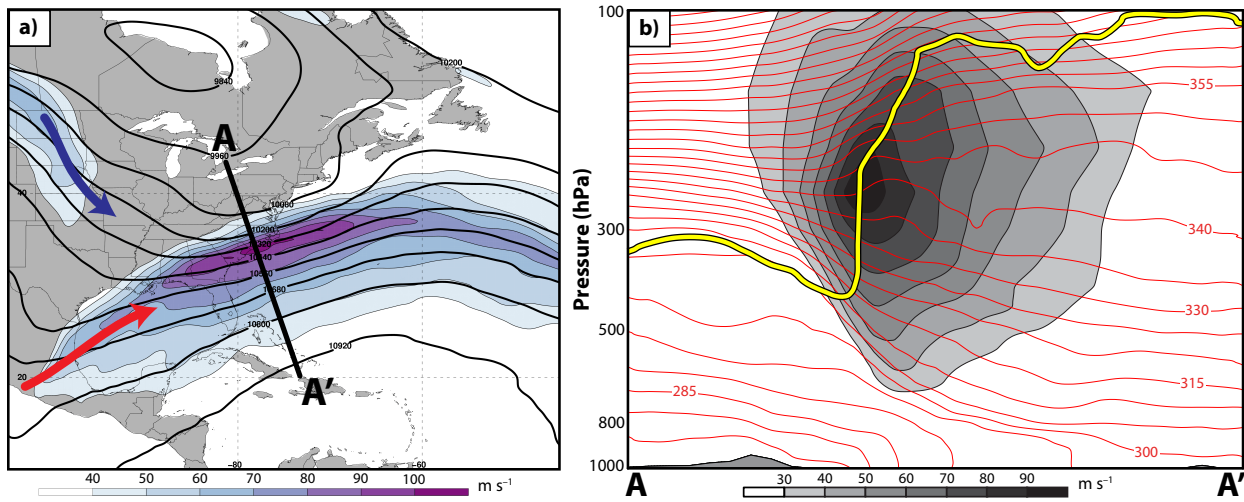
Jet Superposition Characteristics				
	Avg. Starting Latitude	Avg. Starting Longitude	Avg. Δ Latitude	Avg. Δ Longitude
Polar Dominant (N = 80)	29.7°N	102.0°W	+3.42°	+12.25°
Hybrid (N=117)	34.5°N	94.3°W	+0.85°	+11.20°
Subtropical Dominant (N=129)	46.7°N	92.1°W	-0.96°	+12.32°
East Subtropical Dominant (N=76)	48.5°N	71.2°W	-1.13°	+9.56°
West Subtropical Dominant (N=53)	44.0°N	122.1°W	-0.78°	+15.10°

875

876 TABLE 1. Average characteristics of jet superposition events as a function of event type. These
877 characteristics include the average latitude and longitude at which jet superpositions develop for
878 each event type, and the average change (Δ) in latitude and longitude a jet superposition's
879 position during its lifespan for each event type.

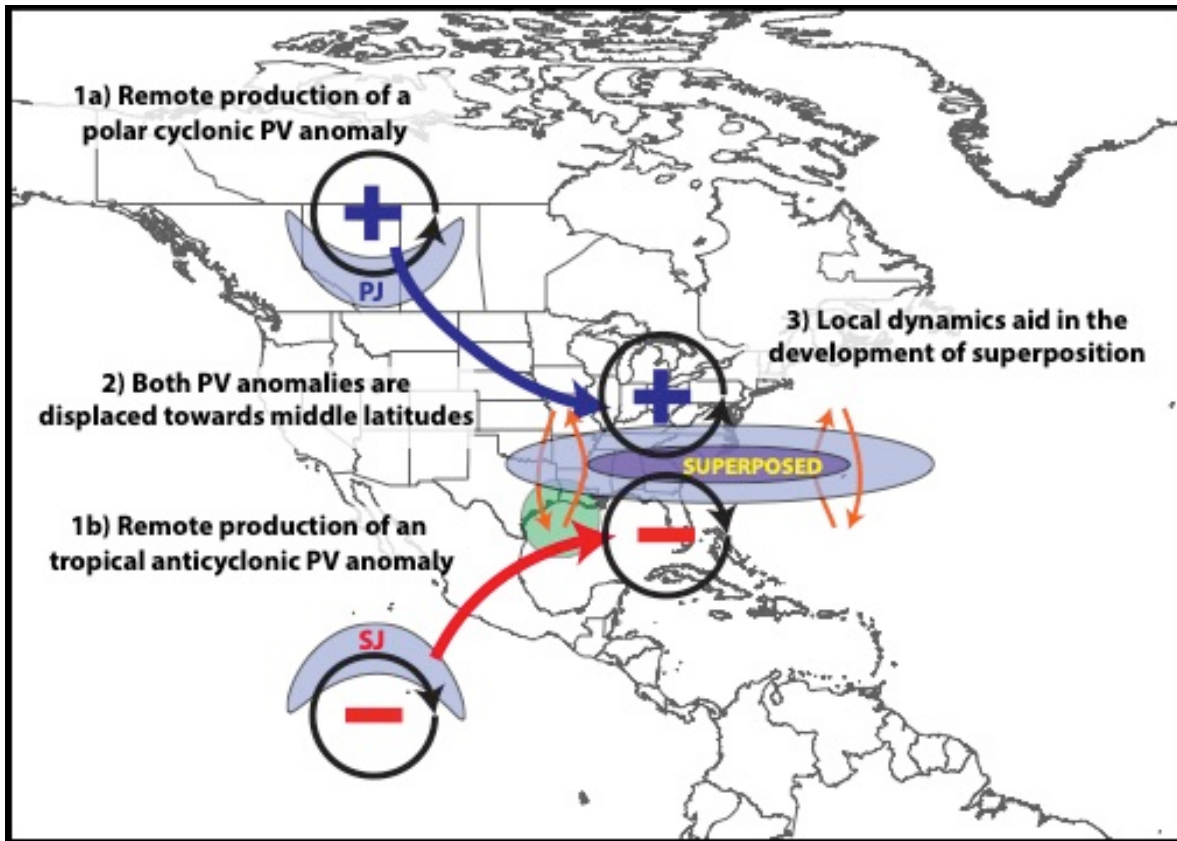
880

881 **Figures**



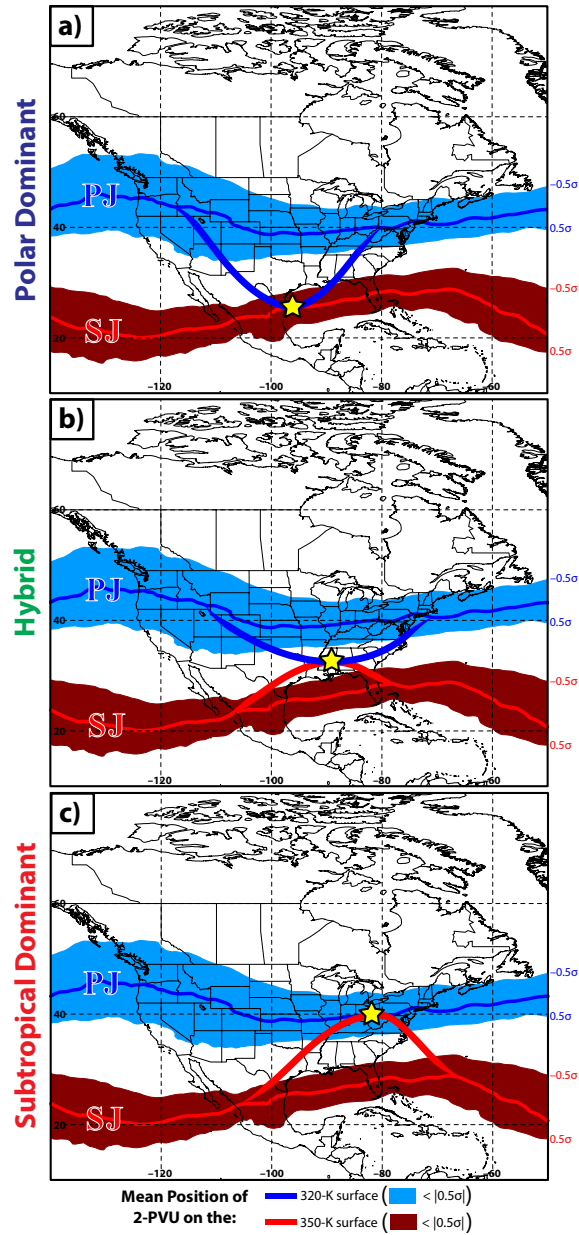
882
883
884
885
886
887
888
889
890

FIG. 1. (a) 250-hPa geopotential height is contoured in black every 120 m and 250-hPa wind speed is shaded in m s^{-1} according the legend at 1200 UTC 20 December 2009. The blue and red arrows identify flow along the polar and subtropical waveguides, respectively. (b) Cross section from A–A', as indicated in (a), of a jet superposition. Wind speed is shaded in m s^{-1} according the legend, potential temperature is contoured in red every 5 K, and the 2-PVU contour is drawn in yellow to highlight the structure of the dynamic tropopause.



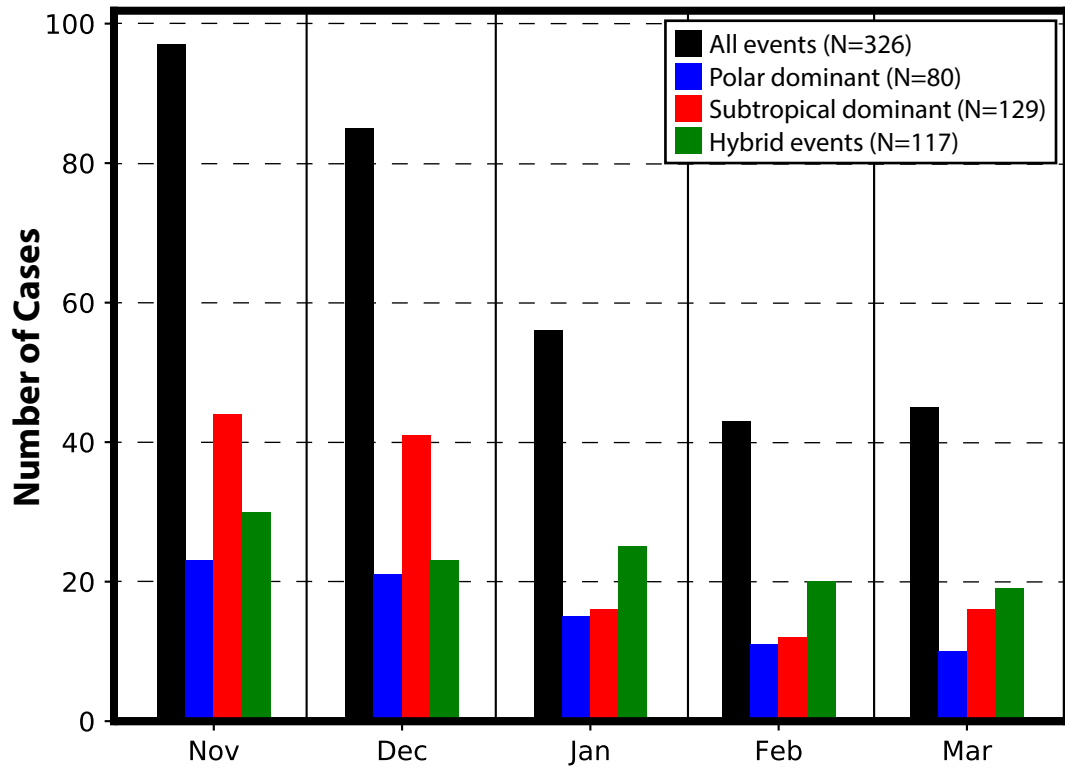
891
 892
 893
 894
 895
 896
 897
 898
 899
 900
 901

FIG. 2. Conceptual diagram summarizing the development of a jet superposition. The orange arrows depict the branches of an across-front ageostrophic circulation, the green circle identifies an area of convection, and the plus (minus) sign corresponds to the center of a polar cyclonic (tropical anticyclonic) PV anomaly, with the blue (red) arrow indicating the movement of that particular PV anomaly toward midlatitudes. The purple fill pattern corresponds to isotachs, with the darker shade of purple identifying faster wind speeds. The locations of the polar jet (PJ), subtropical jet (SJ), and superposed jet are labeled accordingly. Figure and caption adapted from Winters and Martin (2017).



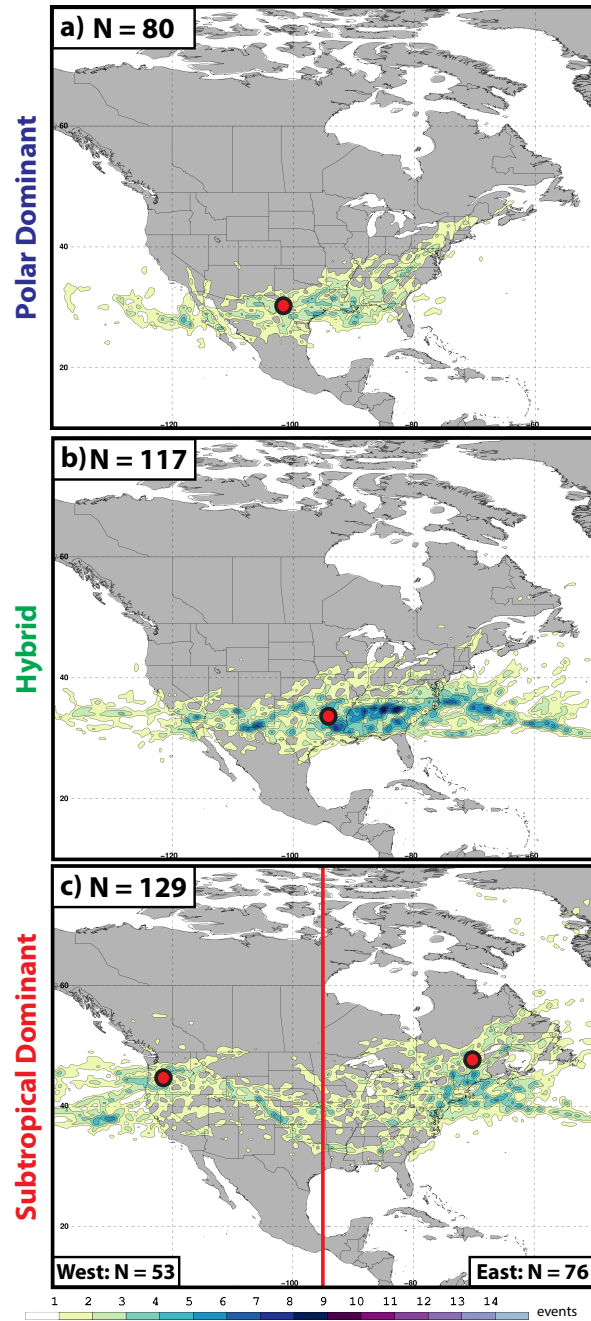
902
 903
 904
 905
 906
 907
 908
 909
 910
 911
 912
 913

FIG. 3. The mean position of the 2-PVU contour on the 320-K and 350-K isentropic surfaces at 0000 UTC 1 January is indicated by the thin blue and red line, respectively, and represents the mean position of the polar (PJ) and subtropical (SJ) waveguides. Shaded areas bounding each mean 2-PVU contour indicate locations at which an observation of 2-PVU on that particular isentropic surface would represent a standardized PV anomaly with a magnitude less than 0.5. Hypothetical deviations of the 2-PVU contour from its mean position on each isentropic surface that result in the formation of (a) a polar dominant jet superposition event (yellow star) are indicated by the thick blue and red contours. (b) As in (a), but for a hybrid event. (c) As in (a), but for a subtropical dominant event.



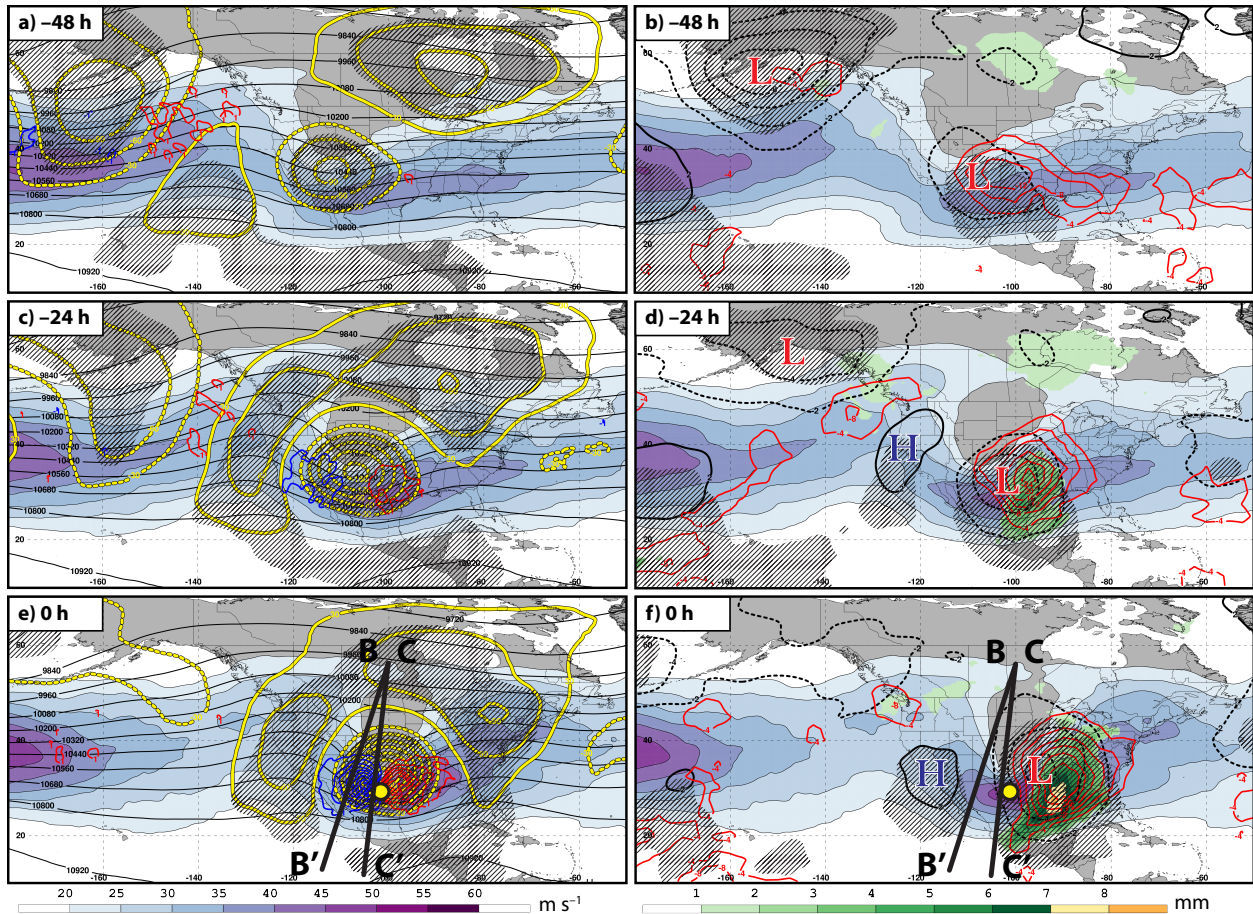
914
 915
 916

FIG. 4. Monthly frequency of jet superposition events as a function of event type.



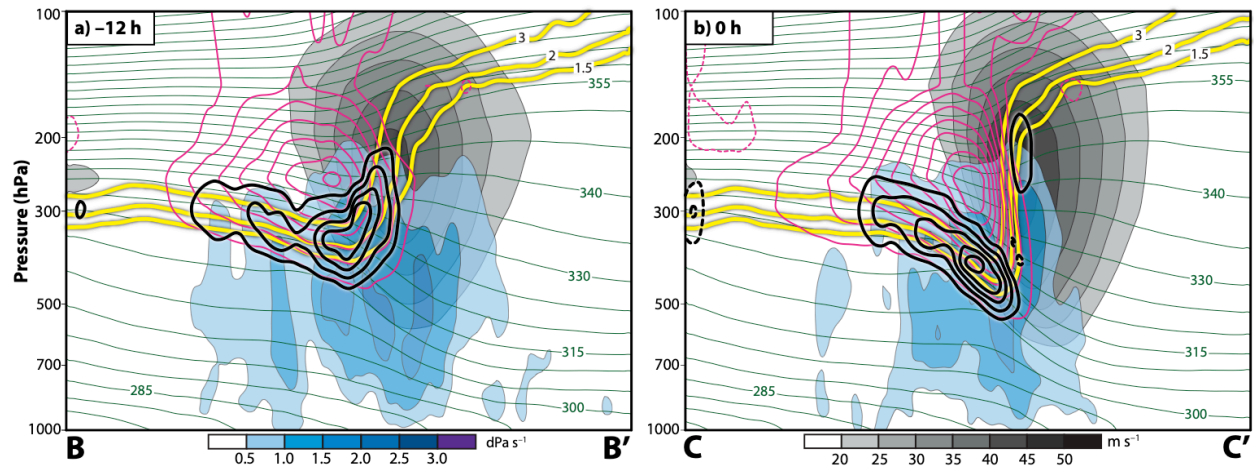
917
 918
 919
 920
 921
 922
 923
 924
 925
 926

FIG. 5. (a) The spatial frequency of polar dominant jet superposition events is shaded following the legend. The red circle represents the average location of jet superposition for polar dominant events, as indicated in Table 1. (b) As in (a), but for hybrid events. (c) As in (a) but for subtropical dominant events. The vertical red bar in (c) is used to illustrate the partition of subtropical dominant events into an eastern and a western category. The red dot to the east (west) of the vertical red line in (c) indicates the average location of superposition for eastern (western) subtropical dominant events.



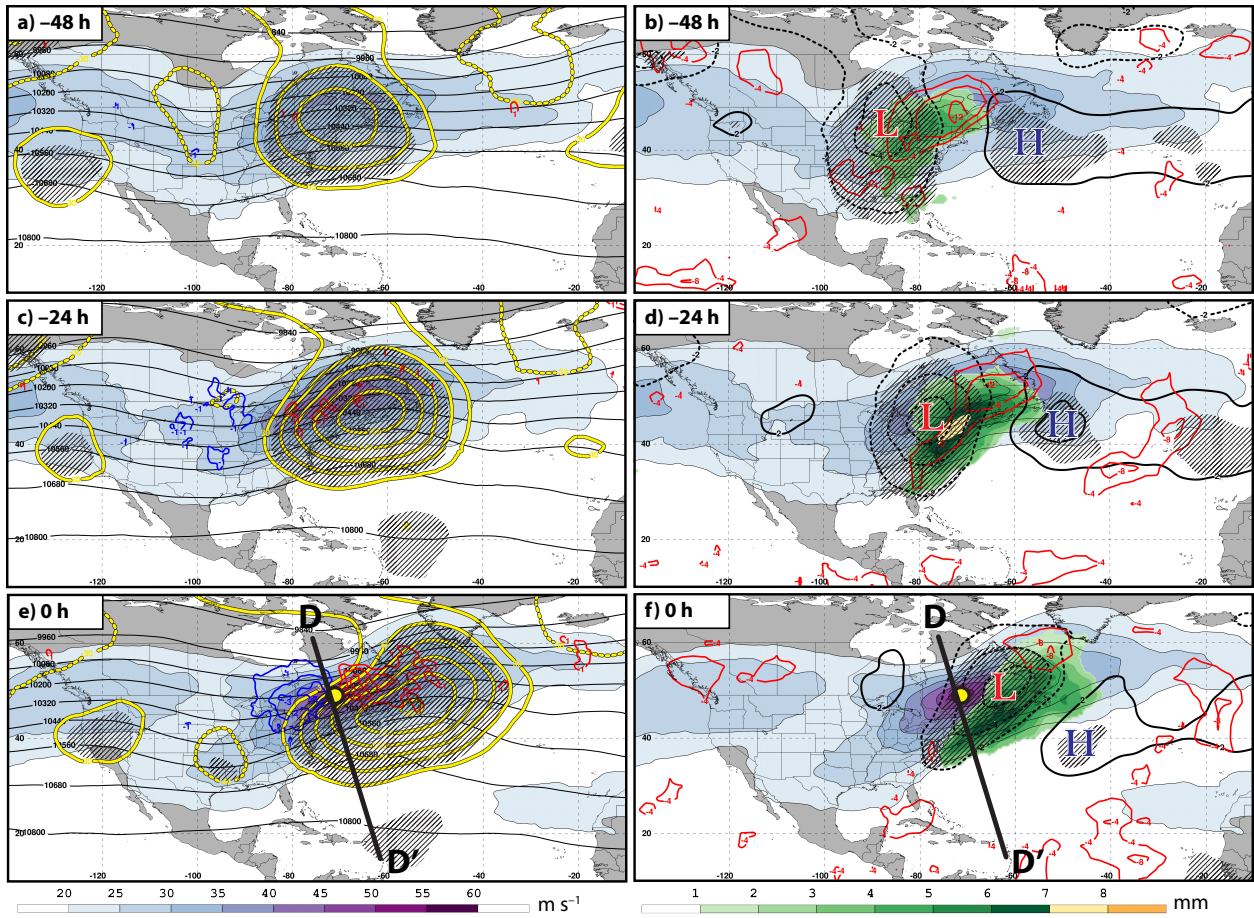
927
928

929 FIG. 6. Composite large-scale flow evolution prior to the initiation of a polar dominant jet
 930 superposition event. (left) 250-hPa geopotential height is contoured in black every 120 m, 250-
 931 hPa geopotential height anomalies are contoured in solid and dashed yellow every 30 m for
 932 positive and negative values, respectively, 250-hPa wind speed is shaded in m s^{-1} according to
 933 the legend, and 300-hPa geostrophic cold- (warm-) air advection is contoured in blue (red) every
 934 $1 \times 10^{-4} \text{ K s}^{-1}$ for (a) 48 h, (c) 24 h, and (e) 0 h prior to jet superposition. Hatched areas
 935 represent locations where the 250-hPa geopotential height anomalies are statistically distinct
 936 from climatology at the 99% confidence level. (right) 250-hPa wind speed is shaded in m s^{-1}
 937 according the legend, mean sea level pressure anomalies are contoured in solid and dashed black
 938 every 2 hPa for positive and negative values, respectively, negative OLR anomalies are
 939 contoured in red every 4 W m^{-2} , and precipitable water anomalies are shaded in mm according to
 940 legend at locations in which they are statistically distinct from climatology at the 99%
 941 confidence level for (b) 48 h, (d) 24 h, and (f) 0 h prior to jet superposition. Hatched areas
 942 represent locations where the mean sea level pressure anomalies are statistically distinct from
 943 climatology at the 99% confidence level. The red “L”s and blue “H”s identify the locations of
 944 surface cyclones and anticyclones.
 945



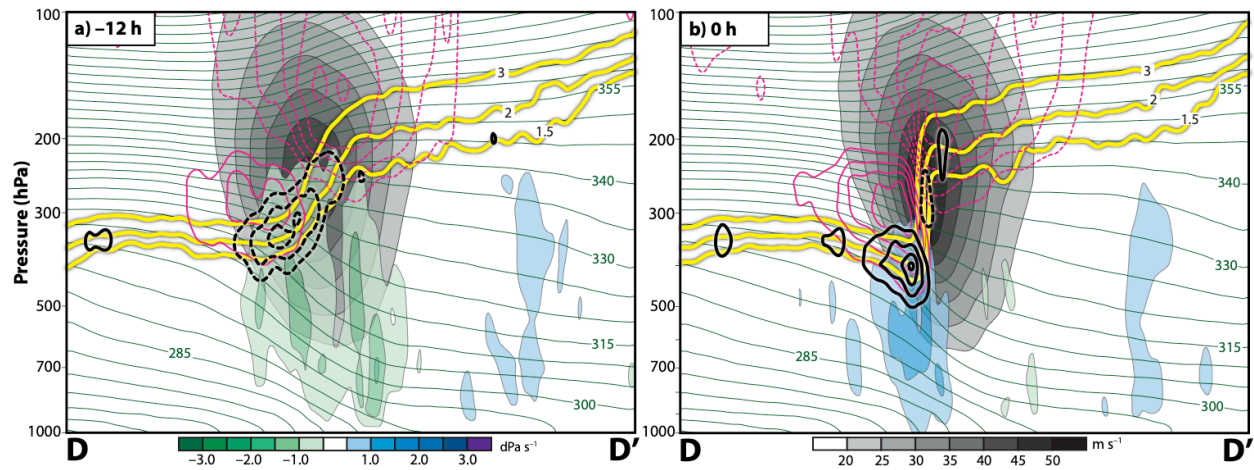
946
 947
 948
 949
 950
 951
 952
 953
 954
 955
 956

FIG. 7. (a) Cross section from B–B', as indicated in Figs. 6e,f, 12 h prior to a polar dominant jet superposition event. Potential temperature is contoured in green every 5 K, wind speed (m s^{-1}) is shaded in grey according the legend, positive (negative) PV anomalies are contoured in solid (dashed) magenta contours every 0.5 PVU, the 1.5, 2-, and 3-PVU contours are indicated in yellow, positive (negative) PV advection accomplished by the divergent wind is contoured in solid (dashed) black contours every $0.5 \times 10^{-5} \text{ PVU s}^{-1}$, and descent (dPa s^{-1}) is shaded in blue according the legend. (b) As in (a), but for the cross section from C–C', as indicated in Figs. 6e,f, 0 h prior to a polar dominant jet superposition event.



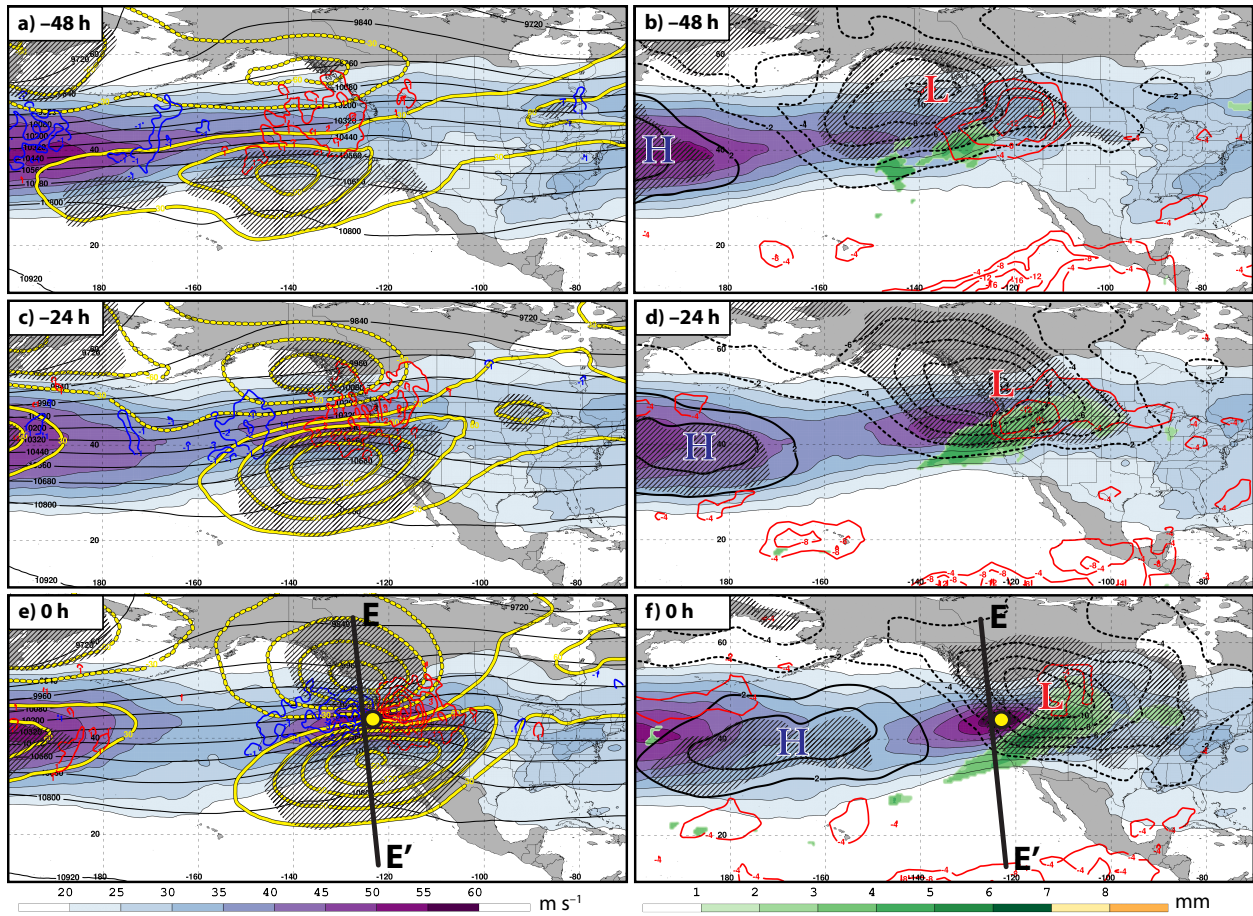
957
 958
 959
 960
 961

FIG. 8. Composite large-scale flow evolution prior to the initiation of an eastern subtropical dominant jet superposition event. All conventions are identical to those in Fig. 6.



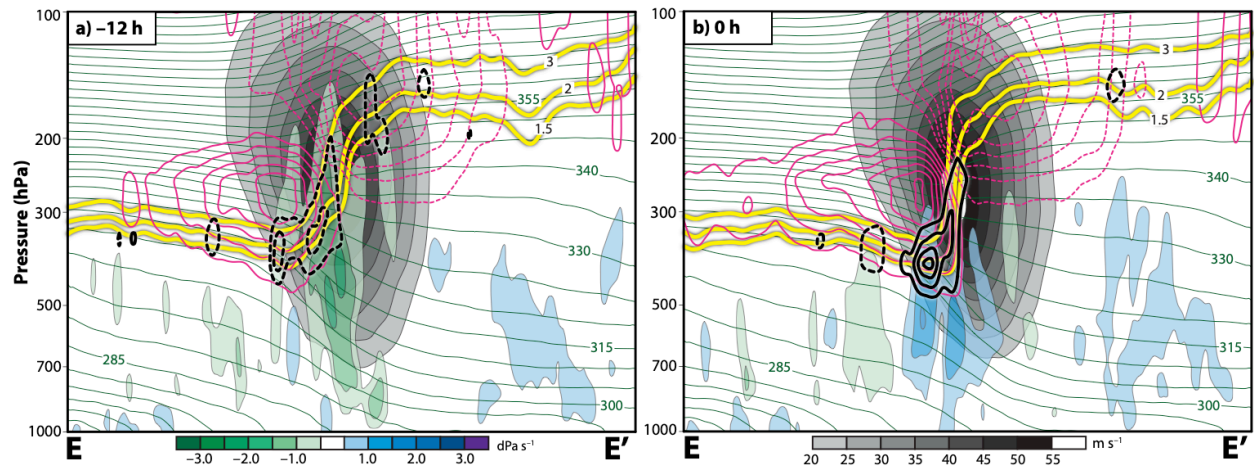
962
963

964 FIG. 9. (a) Cross section from D–D', as indicated in Figs. 8e,f, 12 h prior to an eastern
 965 subtropical dominant jet superposition event. Potential temperature is contoured in green every 5
 966 K, wind speed (m s^{-1}) is shaded in grey according the legend, positive (negative) PV anomalies
 967 are contoured in solid (dashed) magenta contours every 0.5 PVU, the 1.5, 2-, and 3-PVU
 968 contours are indicated in yellow, positive (negative) PV advection accomplished by the divergent
 969 wind is contoured in solid (dashed) black contours every $0.5 \times 10^{-5} \text{ PVU s}^{-1}$, and vertical motion
 970 (dPa s^{-1}) is shaded in blue and green according the legend for descent and ascent, respectively.
 971 (b) As in (a), but for the cross section from D–D', as indicated in Figs. 8e,f, 0 h prior to an
 972 eastern subtropical dominant jet superposition event.
 973



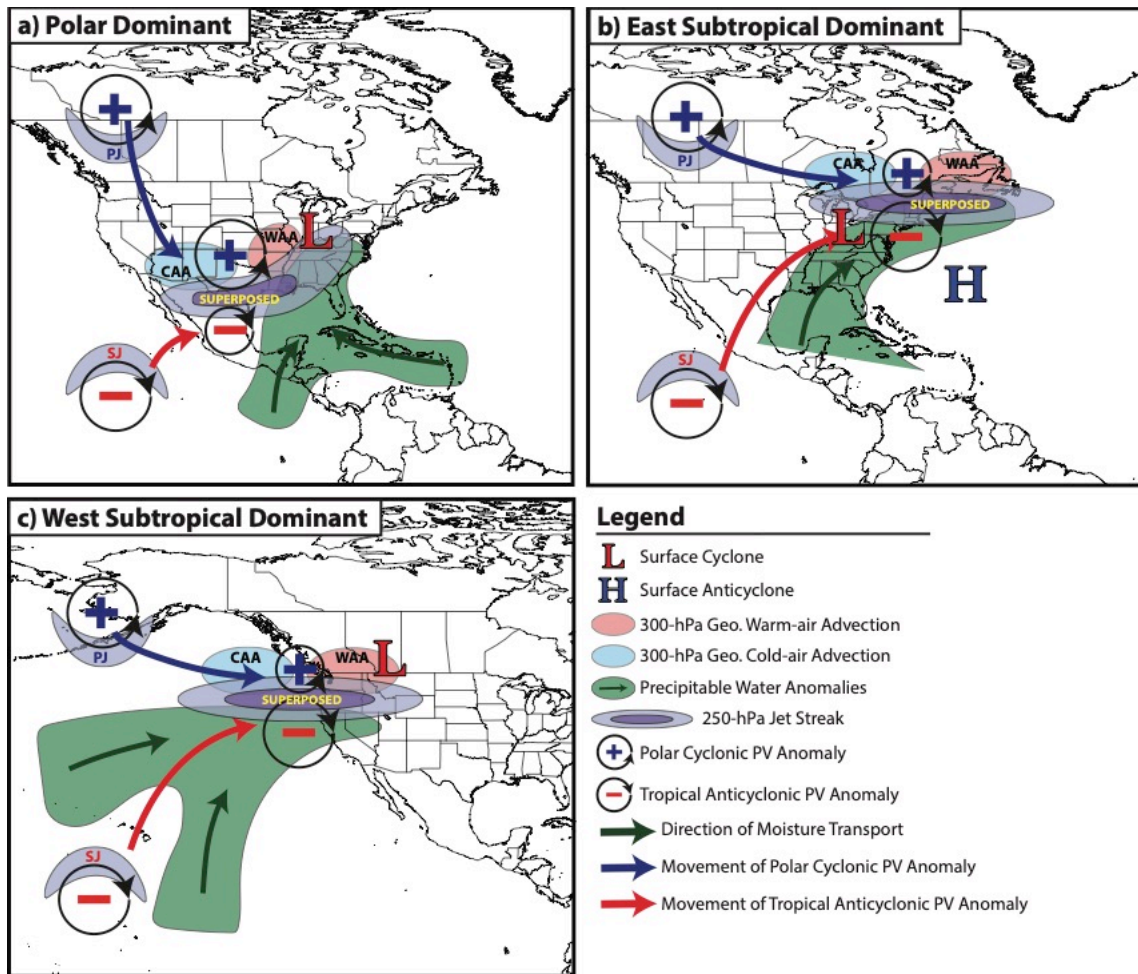
974
 975
 976
 977
 978

FIG. 10. Composite large-scale flow evolution prior to the initiation of a western subtropical dominant jet superposition event. All conventions are identical to those in Fig. 6.



979
 980
 981
 982
 983
 984
 985

FIG. 11. (a) Cross section from E–E', as indicated in Figs. 10e,f, 12 h prior to a western subtropical dominant jet superposition event. All conventions are identical to those in Fig. 9. (b) As in (a), but for the cross section from E–E', as indicated in Figs. 10e,f, 0 h prior to a western subtropical dominant jet superposition event.



986
 987
 988
 989
 990

FIG. 12. Conceptual models for the development of (a) polar dominant, (b) eastern subtropical dominant, and (c) western subtropical dominant jet superposition events.